Validation of O(1S) wind measurements by WINDII: the WIND Imaging Interferometer on UARS

W. A. Gault, Gérard Thuillier, G. G. Shepherd, S.-P. Zhang, R. H. Wiens, C. Tai, B. H. Solheim, Yves Rochon, C. Mclandress, Chantal Lathuillière, et al.

To cite this version:

W. A. Gault, Gérard Thuillier, G. G. Shepherd, S.-P. Zhang, R. H. Wiens, et al.. Validation of O(1S) wind measurements by WINDII: the WIND Imaging Interferometer on UARS. Journal of Geophysical Research: Atmospheres, 1996, 101 (D6), pp.10405-10430. 10.1029/95JD03352 . hal-01627421

HAL Id: hal-01627421
https://hal.science/hal-01627421

Submitted on 6 Feb 2021

JOURNAL OF GEOPHYSICAL RESEARCH, VOL. 101, NO. D6, PAGES 10,405–10,430, APRIL 30, 1996

Validation of O(^{1}S) Wind Measurements by WINDII: the WIND Imaging Interferometer on UARS

W.A. Gault,[1] G. Thuillier,[2] G.G. Shepherd,[1] S.P. Zhang,[1] R.H. Wiens,[1] W.E. Ward,[3] C. Tai,[3] B.H. Solheim,[1] Y.J. Rochon,[1] C. McLandress,[3] C. Lathuillere,[4] V. Fauliot,[2] M. Hersé,[2] C.H. Hersom,[3] R. Gattinger,[5] L. Bourg,[2] M.D. Burrage,[6] S.J. Franke,[7] G. Hernandez,[8] A. Manson,[9] R. Niciejewski[6] and R.A. Vincent.[10]

Abstract. This paper describes the current state of the validation of wind measurements by the wind imaging interferometer (WINDII) in the O(^{1}S) emission. Most data refer to the 90-to-110-km region. Measurements from orbit are compared with winds derived from ground-based observations using optical interferometers, MF radars and the European Incoherent-Scatter radar (EISCAT) during overpasses of the WINDII fields of view. Although the data from individual passes do not always agree well, the averages indicate good agreement for the zero reference between the winds measured on the ground and those obtained from orbit. A comparison with winds measured by the high resolution Doppler imager (HRDI) instrument on UARS has also been made, with excellent results. With one exception the WINDII zero wind reference agrees with all external measurement methods to within 10 m s^{-1} at the present time. The exception is the MF radar winds, which show large station-to-station differences. The subject of WINDII comparisons with MF radar winds requires further study. The thermospheric O(^{1}S) emission region is less amenable to validation, but comparisons with EISCAT radar data give excellent agreement at 170 km. A zero wind calibration has been obtained for the O(^{1}D) emission by comparing its averaged phase with that for O(^{1}S) on several days when alternating ^{1}D/^{1}S measurements were made. Several other aspects of the WINDII performance have been studied using data from on-orbit measurements. These concern the instrument's phase stability, its pointing, its responsivity, the phase distribution in the fields of view, and the behavior of two of the interference filters. In some cases, small adjustments have been made to the characterization database used to analyze the atmospheric data. In general, the WINDII characteristics have remained very stable during the mission to date. A discussion of measurement errors is included in the paper. Further study of the instrument performance may bring improvement, but the utimate limitation for wind validation appears to be atmospheric variability and this needs to be better understood.

1. Background

The wind imaging interferometer (WINDII) was put into orbit on NASA's Upper Research Satellite (UARS) on September 12, 1991. Its mission was to measure winds, temperatures, and emission rates in the altitude range 80 to 300 km, with an emphasis on the lower part of this range. Nearly 16 million images of the upper atmosphere had been acquired up to November 1994, and analysis of the data is in progress. Validation of the results is an essential part of this. In this paper we describe the validation process that was conducted in order to give the reader, including future users of WINDII data, an understanding of the procedures that were employed. Also included is a description of the er-

---

[1] York University, Toronto, Ontario, Canada.

[2] Service d'Aéronomie du CNRS, Verrières-le-Buisson, France.

[3] Institute for Space and Terrestrial Science, Toronto, Ontario, Canada.

[4] Centre d'Etude des Phénomènes Aleatoires et Géophysiques, Saint-Martin-d'Hères, France.

[5] National Research Council, Ottawa.

[6] University of Michigan, Ann Arbor.

[7] University of Illinois, Urbana.

[8] University of Washington, Seattle.

[9] University of Saskatchewan, Saskatoon.

[10] University of Adelaide, Adelaide, Australia.

Paper number 95JD03352.
0148-0227/96/95JD-03352$05.00

ror estimate procedures and estimated error values. A detailed description of the comparison with a ground-based Michelson interferometer is presented in a companion paper by *Thuillier et al.* [this issue]. Preliminary scientific results have been presented by *Shepherd et al.* [1993a], *McLandress et al.* [1994], and *Shepherd et al.* [1995]. The present paper describes the current state of the validation of the winds measured from the O^1S emission and the method used to determine the preliminary zero wind value for the O^1D wind measurements. The validation of other quantities measured by WINDII will be presented in later publications.

The instrument has been described by *Shepherd et al.* [1993b], along with the basic data analysis procedure. A field-widened Michelson interferometer [*Hilliard and Shepherd*, 1966] is positioned in the optical path of a charge coupled device (CCD) imager directed toward the Earth's limb with the bottom of the image corresponding to a tangent point altitude of about 80 km and the top at about 300 km. Single airglow emission lines are isolated with interference filters, so that an image obtained from that emission is an image of the emission rate multiplied by the transmittance of the interferometer, which depends on its phase setting as well as on its off-axis phase variation. One mirror of the interferometer is phase stepped as an image sequence is acquired, either four or eight steps to cover one complete fringe. For each pixel on the image the corresponding eight signal values are analyzed to determine the phase of the cosinusoidal signal. The principle of wind measurement from space consists of comparing the phase generated by an airglow line with the phase in the same instrumental condition when there is no Doppler shift of the wavelength of this line. Let the ϕ be the phase of the emission between 0 and 2π and let $\phi_{\rm int}$ be this intrinsic phase when the wind is null. The wind velocity is then given by $v = K_1 \ (\phi - \phi_{\rm int})$, where K_1 is the constant $\frac{\lambda_o c}{2\pi D}$. Here, λ_o is the unshifted wavelength of the emission, c is the velocity of light, and D is the effective optical path difference of the interferometer as given by *Thuillier and Hersé* [1991].

As the zero wind phase is not available in orbit, a calibration lamp delivering a line of wavelength close to λ_o is used, providing a phase ϕ_c. Calibration on the ground consists in measuring $\phi_{\rm int} - \phi_c$ by the use of the same lamp as in orbit and a source delivering the same airglow line as in the Earth's atmosphere. The fundamental principle of the wind measurement is to assume that

$$(\phi_{\rm int} - \phi_c)_{\rm orbit} = (\phi_{\rm int} - \phi_c)_{\rm ground} = \phi_z \qquad (1)$$

ϕ_z is assumed to be a constant from ground to space. It needs to be known for the two instrument fields and for both day and night apertures. Operating the calibration lamp at regular intervals in orbit provides ϕ_c, allowing the reconstruction of the zero wind phase in orbit from $\phi_z + \phi_c$ and its trend during the mission. The purpose of the validation is to estimate the magnitude of the errors, and this is discussed in detail below.

In practice, it is more complicated than this. First of all, since we are dealing with images, $\phi_{\rm int}$ is an image $\phi_{\rm int}(k,l)$, where k and l represent CCD rows and columns, respectively. In addition, WINDII has two fields of view, one at 45° and the other at 135° to the spacecraft velocity vector, in order to measure two components of the horizontal wind; the fields of view have independent $\phi_{\rm int}(k,l)_1$ and $\phi_{\rm int}(k,l)_2$ images. As well, WINDII uses a stopped-down aperture during the daytime to accommodate the baffle system which screens the light from the bright cloud tops below. Since only a portion of the full Michelson interferometer aperture is used in this case, the phase condition is different from that at night, and so there are two different zero images for each field of view, e.g., $\phi_{\rm int}(k,l)_2^D$ and $\phi_{\rm int}(k,l)_2^N$ for field of view 2 (FOV2). Finally, the spacecraft velocity component along the line of sight must be removed, as well as that of the Earth's rotation velocity.

The WINDII instrument has an extensive package of calibration equipment, intended to provide a basic characterization capability in orbit. This includes four spectral lamps for phase calibration in each of the four spectral regions, a tungsten lamp for responsivity calibration and a laser for the calibration of visibility, which is a measure of the interferometer's ability to modulate emission lines. The stabilized He-Ne laser is in itself a primary standard of visibility.

The spectral lamps and the tungsten lamp are considered secondary standards that were calibrated against primary standards on the ground. The primary standards for phase (zero wind) were laboratory lamps emitting the same atmospheric emission lines as observed in flight. Preflight ground characterization also included measurement of the filter passbands for each elementary bin on the CCD.

In addition to showing general consistency with other methods of measuring the wind, there were several specific reasons to conduct in-flight validation of the data. Calibration measurements are particularly difficult with an interferometer having a large field of view, and there is the possibility of sudden changes occurring during launch and gradual ones afterward in the space environment. The laboratory sources of atmospheric lines could have had undetected parasitic lines able to induce some systematic phase error. Also, only one of the two instrument fields of view was calibrated with the atmospheric line source, and this calibration was then transferred to the other field, assuming symmetry in the interferometer. This procedure may have introduced some error. Atmospheric observations made at the Earth's limb require the deconvolution of one or several integral equations as a function of altitude. In the case of WINDII, three equations are solved by a method explained by *Shepherd et al.* [1993b]. All of the above considerations led to the necessity of having a campaign of correlative measurements between WINDII in orbit and other instruments.

Important comparisons were made with a similar Michelson interferometer using the same O^1S emission line, the MICADO instrument operated at the Observatoire de Haute-Provence. Other optical comparisons were made with the same emission line but against a different type of instrument, Fabry-Perot interferometers operated at Mount John in New Zealand and at Peach Mountain in Ann Arbor, Michigan. Another type of comparison was made with the high-resolution Doppler imager (HRDI) on UARS [*Hays et al.,* 1993], which measures winds from a different emission, the O_2 atmospheric band. Finally, comparisons were made against measurements by nonoptical methods, namely, radars. There is an extensive worldwide network of MF radars, and for these comparisons, sites were selected in Adelaide, Christmas Island, Saskatoon, and Urbana. In addition, the European incoherent-scatter (EISCAT) facility provided incoherent scatter wind comparisons, including an important one at 170 km. All of the WINDII data reported here have been analyzed using version 4.23 of the production software.

2. Wind Measurement Procedure

2.1. Instrument Description

Light entering WINDII passes first through a large (~1 m) baffle, then through a telescope, a filter, another telescope, the Michelson interferometer, and finally is focused at the CCD detector by a camera lens. The first telescope has two objective lenses and a double mirror which combines the two fields of view into one, so they appear side by side on the CCD. The second telescope contains the actual field stop. The filter wheel has eight positions, one of which is open to allow for calibrations and the imaging of star fields. The other seven positions contain interference filters for the various atmospheric emissions and background measurements. Several plane mirrors are used to fold the optics into a compact form. The look directions for the two fields of view are approximately normal to each other, viewing the atmosphere at the limb on the antisunward side of the spacecraft, at 45° and 135° to the velocity vector. Diagrams of the instrument and optical system are given by *Shepherd et al.* [1993b].

During calibrations, two mirrors are deployed, one in front of each entrance aperture and at 45° to the optical axis, cutting off light from the atmosphere and allowing the instrument to view the calibration sources. Phase calibrations and dark current measurements are done approximately every 15 to 20 min. Major calibrations, including responsivity (tungsten lamp) and visibility (He-Ne laser) as well as phase (spectral lamps), are done about once per week.

The baffle is designed to permit daytime measurements of the weak airglow emissions, which can appear as closely as 1.5° above the sunlit cloud layers. This design includes a retractable stop which reduces the entrance aperture to a narrow slot during the daytime in order to prevent the sunlight scattered by the cloud layers from entering directly into the WINDII optical system. We refer to these two configurations as the "day aperture" and the "night aperture". The reduced collecting area during the daytime is approximately compensated by the increased emission rate.

The Michelson interferometer is achromatically field widened and thermally compensated and set at a path difference of 4.46 cm. With a larger path difference than this, the fringes due to the hot thermospheric emissions (O ^{1}D and O^+ ^{2}P) would lose visibilty and their wind measurements would be compromised. The Michelson consists of hexagonal beam splitter and two arms of different glasses with a small gap at the end of one arm. The mirror in this arm is piezoelectrically mounted for alignment adjustment and changing the path difference in the small steps required to measure the phase and visibility of the fringes. The whole interferometer is cemented together, forming a very rugged unit.

To limit the amount of data for transmission and improve the signal-to-noise ratio, the CCD pixels are grouped together in bins and the signals are added on the chip for each bin. Most measurements are made using six columns of bins, each 25 pixels wide and 2 to 8 pixels high. Observing windows are also defined for the CCD, including only the parts of the CCD where useful data are obtained. The fields of view are fixed with respect to the spacecraft, so the emission layers rise and fall in the CCD image as the spacecraft changes altitude, and the windows move up and down accordingly. Typical exposure times for the ^{1}S emission are 1 to 2 s.

2.2. Data Analysis

Analysis of WINDII data begins at the level of the individual bins which compose the phase images. Each bin measures a line-of-sight intensity of the airglow limb. The altitude associated with a bin is the altitude at the tangent point. Thus a column of bins scans a vertical slice in the atmosphere with an altitude range defined by the bottom and top bins in the column. The horizontal extent is normally the full width of the image area, which maps to about 140 km at the tangent points along a row of bins. A single pixel subtends approximately 1 km^2 at the tangent point giving a vertical resolution of 2 km for a two-pixel bin. The bin size is chosen to give optimum signal to noise ratio and spatiotemporal resolution for a given observation.

A measurement contains the atmospheric signal as well as a background signal. During normal operations a background image is taken followed by a set of phase images. The processing software subtracts the appropriate dark current from the background and atmospheric images bin by bin. The raw count rate is next converted to geophysical units (Rayleigh) using the responsivity of each bin. (One Rayleigh corresponds to an emission of 10^6 photon s^{-1} from a 1 cm^2 column along the line of sight.) This calibration information is stored in a characterization database (CDB) which is accessed by the production processing software. Since the background is taken at a different wavelength (552.5 nm) than the atmospheric line of interest, the background image is corrected to the observation wavelength. The method used to correct the background image is described by *Shepherd et al.* [1993b]. The corrected background is then subtracted from each of the measurement images yielding only the atmospheric signal.

WINDII views the limb and so is sensitive to the spacecraft attitude. The altitude, latitude, and longitude of each bin in each image are computed. Either four or eight images are taken for a normal measurement. The observatory may roll or change attitude from image to image. Using a middle image in a set of 4 or 8 to give a reference altitude, the remaining images are corrected to account for any attitude variation. Next the velocities due to spacecraft motion and earth rotation, projected along the line of sight, are derived for each bin. These are used to calculate the contribution to the observed phase of the spacecraft-induced Doppler shift. The instrument phase determined from the frequent phase calibration is corrected from the CDB to give the zero wind phase for the current measurement. Finally the projected velocity phase and the zero wind phase are combined with the mirror step phase to give the known phase component of the measurement.

The measured intensity of a given bin at a given time may be written in the generalized form as an integral along the line of sight L:

$$I_p = \int_L E(z)\,[1 + UV(z)\cos(\Phi_p + \phi_w(z))]\,dl \quad (2)$$

where $E(z)$ is the volume emission rate at altitude z, U is the intrinsic (instrumental) visibility of a given bin, $V(z)$ is the line visibility corresponding to the atmospheric temperature, $T(z)$ and $\phi_w(z)$ is the phase due to the atmospheric wind; $\Phi_p = \mathit{\Phi} + (p - 1)\varphi$, where $\mathit{\Phi}$ is the phase due to the optical path difference, spacecraft velocity, and Earth rotation, φ is the step size for the Michelson mirror, and the index $p = 1, 2, \cdots, n$, where n is the number of steps per measurement. Usually, $\varphi = \frac{2\pi}{n}$. The relationship between $V(z)$ and $T(z)$ is given by

$$V(z) = e^{-Q\Delta^2 T(z)} \quad (3)$$

where Δ is the optical path difference in the interferometer and Q is a molecular constant [*Hilliard and Shepherd,* 1966].

If the cosine argument is expanded, then equation (2) may be written as

$$\begin{aligned} I_p &= \int_L E(z)dl \\ &+ U\cos\Phi_p \int_L E(z)V(z)\cos(\phi_w(z))dl \\ &- U\sin\Phi_p \int_L E(z)V(z)\sin(\phi_w(z))dl \quad (4) \end{aligned}$$

$$I_p = J_1 + U\cos\Phi_p J_2 - U\sin\Phi_p J_3 \quad (5)$$

The values J_1, J_2, and J_3 are the line integrals in equation (4) and contain the atmospheric information we wish to recover. The vectors J_1, J_2 and J_3 are defined to be the "apparent quantities." Equation (5) thus forms a simple linear system which is solved with standard matrix techniques.

Wave motion, or other structure in the atmosphere, perturbs the interferogram and thus introduces error in the recovered wind. The magnitude of this error is reduced by combining the six columns in a typical image across each row to give one vertical column or one profile for each field of view. This column combination also reduces the random error relative to a single bin. The final result provides two column vectors referenced to the centers of each field of view for each of J_1, J_2, and J_3. These are the apparent quantities that are used in the inversion routine.

A locally spherically uniform and time invariant atmosphere is assumed for the inversion of the apparent quantities; the inversion might not correctly recover the atmospheric information in regions of significant inhomogeneity, for example, in twilight or in regions of auroral activity. Each profile for each field of view is inverted separately using a linear constrained least squares method with statistical weighting [*Menke,* 1984; *Twomey,* 1977]. Linear constraints are introduced for damping noise-related oscillations. Data reduction, including the inversion process, is further summarized in section 3 within the context of a random error assessment. There is always a trade-off between noise reduction and the smoothing of vertical structures. The weighting factors and the constraint matrices have been chosen to reduce noise but not to remove real atmospheric structure.

Once the volume emission rate, wind, and temperature profiles have been obtained from each field of view, the meridional and zonal wind components are derived by combining forward and backward looking observations. The two fields of view track each other through the atmosphere. Approximately 7 min after the forward field of view sees a particular volume of air, the backward looking view sees the same volume from a perpendicular direction. The line of sight winds are combined to yield the vector winds only if the two views intersect within 300 km at the tangent points. The volume emission rate and the wind from the two fields are averaged to give the final profiles at the intersection point. Before averaging the scalar quantities or resolving the wind vectors, the profiles are all interpolated to a common altitude grid. The final step in the processing is to reduce random noise without removing discernible atmospheric structures.

2.3. Instrument Characterization

The ground characterization of WINDII took place during September and October, 1990, approximately one year prior to launch. This was an effort to measure all the characteristics of the instrument that would be needed to create the CDB, which is used to support operational data processing. A full discussion of the characterization is given by *Hersom and Shepherd* [1995]. Among the quantities measured were the zero reference phase for O^1S and the responsivity.

A small laboratory source of O^1S emission was developed by Resonance Incorporated, to determine the interferometer's phase corresponding to zero Doppler shift. The limitations of the low intensity of the 557.7-nm emission and the need to block a nearby contaminant line meant that the entrance aperture could be fully illuminated for only a portion of the field of view. Thus the zero was determined for a region near the bottom of the field, and a rubidium lamp, with an isolated emission line at 557.9 nm, was used to provide the phase distribution over the rest of the field as well as the phase shift between day and night aperture settings. In addition, phase measurements were made using the onboard krypton calibation lamp (557.0 nm) so that $(\phi_{\mathrm{int}} - \phi_c)_{\mathrm{ground}}$ could be determined for O^1S. No laboratory source was available for the O^1D emission at 630.0 nm, but the phase distribution over the field and the difference in phase between day and night apertures was determined using the neon line at 630.5 nm.

The responsivity measurement utilized a calibrated tungsten-halogen lamp to irradiate a barium sulfate reflectance screen placed in front of the instrument in such a way that both the aperture and the field of view were completely filled. The lamp was located about 8 m from the reflectance screen to ensure good uniformity of illumination. For each interference filter and both aperture positions a series of exposures was taken with the integration time incremented by 0.25 s from 0.25 s to the saturation point. This provided about 10 measurements for each case. For these measurements the signal was integrated in standard CDB bins of 1×5 pixels, with the long sides horizontal. Thus each image consisted of 240 rows and 31 columns of bins in each of the two fields of view. A least squares linear fit was applied to each data set to determine the signal versus exposure coefficient for each bin. The light level illuminating the aperture was computed in Rayleigh from the known transmission characteristics of the filter, the reflectance of the screen, and the lamp calibration. The instrument responsivity was then determined in ADU s^{-1} $\mathrm{Rayleigh}^{-1}$, where an ADU (analog-to-digital unit) corresponds to one level of digitization.

3. Wind Random Error Assessment

3.1. Introduction

WINDII data provided in the UARS database contain information on the precision of the wind measurements. In this section the sources of random errors in the determination of WINDII winds are reviewed. For clarity, errors affecting the line of sight or apparent quantities are first discussed followed by a summary of the errors associated with the inverted quantities. This approach provides an understanding of the physical sources and causes of the errors which would be masked if only inverted quantities were discussed.

The quantity directly measured by WINDII is a line of sight emission rate (integrated through the emission layer) modulated by the interferometer. The line of sight or apparent phase is calculated by solving a matrix equation formed using sequences of these line of sight modulated emission rates. The associated inverted quantities are calculated from the apparent quantities using linear constrained least squares inversions with statistical weighting, as described in section 3.3. Associated with the derived quantities resulting from each of these steps is a statistical uncertainty in the derived quantitity. These are termed random errors. Apart from the inverted quantities, the variances of these errors are calculated, using standard methods, from the error variances of the variables on which the derived quantity is dependent. More formally, for any solution vector quantity, $\mathbf{f} \equiv \mathbf{f}(\mathbf{x}_i)$, dependent on vectors $\mathbf{x}_i$, the expression

$$\mathbf{f} = \overline{\mathbf{f}} + \sum_i \mathbf{D}_i \varepsilon_i \tag{6}$$

follows from a first-order expansion of $\mathbf{f}$ in terms of the $\mathbf{x}_i$. Here, $\overline{\mathbf{f}}$ is an appropriate reference value for $\mathbf{f}$, the $\mathbf{D}_i$ are coefficient matrices termed contribution functions [*Rogers*, 1976, 1990], the $\varepsilon_i \equiv \hat{\mathbf{x}}_i - \langle \mathbf{x}_i \rangle$ are independent error vectors, and the $\hat{\mathbf{x}}_i$ are measured estimates for the actual values for $\mathbf{x}_i, \langle \mathbf{x}_i \rangle$. The correlation matrix for $\mathbf{f}$ is given as

$$\mathbf{S_f} = \sum_i \mathbf{D}_i \mathbf{S}_{\varepsilon_i} \mathbf{D}_i^T \tag{7}$$

and the variance is

$$\sigma_{f_i}^2 = S_{f\,ii} \tag{8}$$

Here $S_{\varepsilon_{i_{jk}}} = \overline{\varepsilon_{i_j} \varepsilon_{i_k}}$, $S_{\varepsilon_{i_{kk}}} = \sigma_{\varepsilon_{i_k}}^2$.

3.2. Apparent Quantities

The derivation of the apparent quantities proceeds from the analysis of a series of n emission rate images each at a Michelson phase (to within experimental error) Φ_p (section 2.2). Considering the uncertainties of the various parameters in the interferometer equation at each bin, equation (5) is rewritten as

$$\begin{aligned} b_p &= I_p + \varepsilon_{b_p} \approx y_1 \\ &+ y_2 \left(U + \varepsilon_U\right) \cos\left[(p-1)\left(\varphi + \varepsilon_\varphi\right) + \left(\Phi + \varepsilon_\Phi\right)\right] \\ &- y_3 \left(U + \varepsilon_U\right) \sin\left[(p-1)\left(\varphi + \varepsilon_\varphi\right) + \left(\Phi + \varepsilon_\Phi\right)\right] \end{aligned} \tag{9}$$

where

$$\begin{aligned} y_1 &= J_1 + \varepsilon_{y_1} \\ y_2 &= J_2 + \varepsilon_{y_2} \\ y_3 &= J_3 + \varepsilon_{y_3} \end{aligned} \tag{10}$$

The values of ε_x denote deviations from the corresponding true values and $(I_p + \varepsilon_{b_p})$, $(U + \varepsilon_U)$, $(\varphi + \varepsilon_\varphi)$ and $(\Phi + \varepsilon_\Phi)$ are, respectively, the available estimates of the emission line signals, instrument visibility, incremental phase step, and phase (excluding ϕ_w). The J values are as defined earlier (equations (4) and (5)). Applying the small-angle approximation to the phase errors yields to first order an expression which may be used to form a matrix equation for the set of n images. The apparent quantities and the associated covariances are determined from the weighted least squares method. It is of some interest to note the equivalence of this approach for the unweighted case (originally discussed by *Wiener* [1930]) to the discrete Fourier transform for an even number of equally spaced steps in an interval of 2π.

Upon solving the above system, the Doppler wind phase variance for four phase steps of $\pi/2$ or eight phase steps of $\pi/4$ is given as

$$\sigma^2_{\varphi_w} = \sigma^2_\Phi + \frac{2c_T}{U^2 n \overline{T}_r n_A} \frac{\left(y_1 + \frac{I_B + (C_D - C_{\text{bias}})c_T}{T_f} + \frac{c_T \sigma_R^2}{T_f} \right)}{(y_2^2 + y_3^2)} \tag{11}$$

where the effect of the phase step uncertainty has been neglected. Here, c_T is the conversion factor transforming the raw count (ADU) to Rayleigh, T_f is the mean filter transmittance over the measurement being considered for the emission being observed (i.e., 557.7 nm), n_A is the raw count to electron conversion factor (= 73 e ADU^{-1}), I_B is the background signal in Rayleigh, C_D is the dark count, and C_{bias} is the bin bias, both in ADU, and σ^2_Φ is the net random error variance associated with the intrinsic phase; σ^2_R is termed the reading error variance (ADU) and consists of the readout (50 e), digitization (21 e) and on-chip noise (62 e) contributions. The relationship between the Doppler wind phase ϕ_w and the Doppler wind w is

$$\phi_w + \varepsilon_{\phi_w} = 2\pi \frac{D}{\lambda_o} \frac{(w + \varepsilon_w)}{c} \tag{12}$$

Neglecting the small uncertainty of the conversion parameters, the Doppler wind error variance is

$$\sigma^2_w = \sigma^2_{\phi_w} \left(\frac{c\lambda_o}{2\pi D} \right)^2 \tag{13}$$

where D is the effective path difference as defined by *Thuillier and Hersé* [1991].

The two main sources of error variance appearing in equation (11) are those associated with the emission rate measurements (first term on the right) and those associated with the phase determination (the second term on the right-hand side of equation (11)), termed the intrinsic phase error variance. The shot noise associated with the measurement process itself (for the green line, the background and the dark count measurements all make a contribution) is the main source of error variance for the emission rate measurements except when the observed emission rate is small. In this case the reading error is also significant.

The intrinsic phase total error variance is composed of terms associated with the calibration lamp phase measurements, the relative phase difference (the phase difference between the reference lamp and the observed emission), the phase associated with the satellite velocity, and the phase associated with the Earth's rotation. For the most part the first two error variance sources comprise the dominant contribution. Not included in this phase error variance, as mentioned above, is a contribution due to the uncertainty in the interferometer phase step between images. This contribution varies depending on the value of ϕ [*Ward,* 1988] and has a maximum contribution of 4 m s^{-1} assuming a phase step uncertainty of 0.0005 nm.

The determination of the apparent quantities proceeds on a bin-by-bin basis and results in six profiles of each of the three apparent quantities. As stated in section 2.2, these $\mathbf{y}$ values are averaged over the six measurement columns for each field of view. This scales the size of the resultant random error covariances by 1/6. However, the systematic error covariances are unaffected. Grouping the apparent quantities of the measurement rows, following column averaging, yields three apparent quantity profiles or vectors $\mathbf{y}_i$ and corresponding covariance matrices $\mathbf{S}_{y_{ij}}$, where i and j = 1, 2, and 3.

Figure 1 shows the apparent wind error standard deviations and apparent emission rate profiles for column-averaged quantities associated with typical day (Figures 1a and 1b respectively) and night observations (Figures 1c and 1d) respectively) of the oxygen green line emission with WINDII. In the plots of the apparent emission rate both the emission profile and the background apparent emission rate profile are shown. During the daytime the rapid increase in background apparent emission rate at the lower altitudes due to Rayleigh scattering is evident. In the plots of the apparent wind error standard deviation the error associated with the shot noise (designated s), the reading wind error (designated r), the intrinsic random error, and the total random error are shown. In general, for both day and night the dominance of the error by the shot noise, when the apparent emission rate is high, is apparent. The reading wind error is significant at all heights but is more significant when the apparent emission rate is low. The remaining contribution, the intrinsic wind random error, is due to the satellite and Earth rotation velocity determination ($\sqrt{\sigma^2_{v_s} + \sigma^2_r} = 0.1$ m s^{-1}), the zero wind determination ($\sigma_z = 0.7$ m s^{-1} for the mesosphere and 0.5 m s^{-1} for the thermosphere), and the calibration phase determination ($\sigma_c = 0.3$ m s^{-1}). The intrinsic wind random error is only significant in regions where the apparent emission rate is high.

3.3. Inverted Quantities

The reduction from line-of-sight integrated quantities to profiles in altitude is performed using three inversions

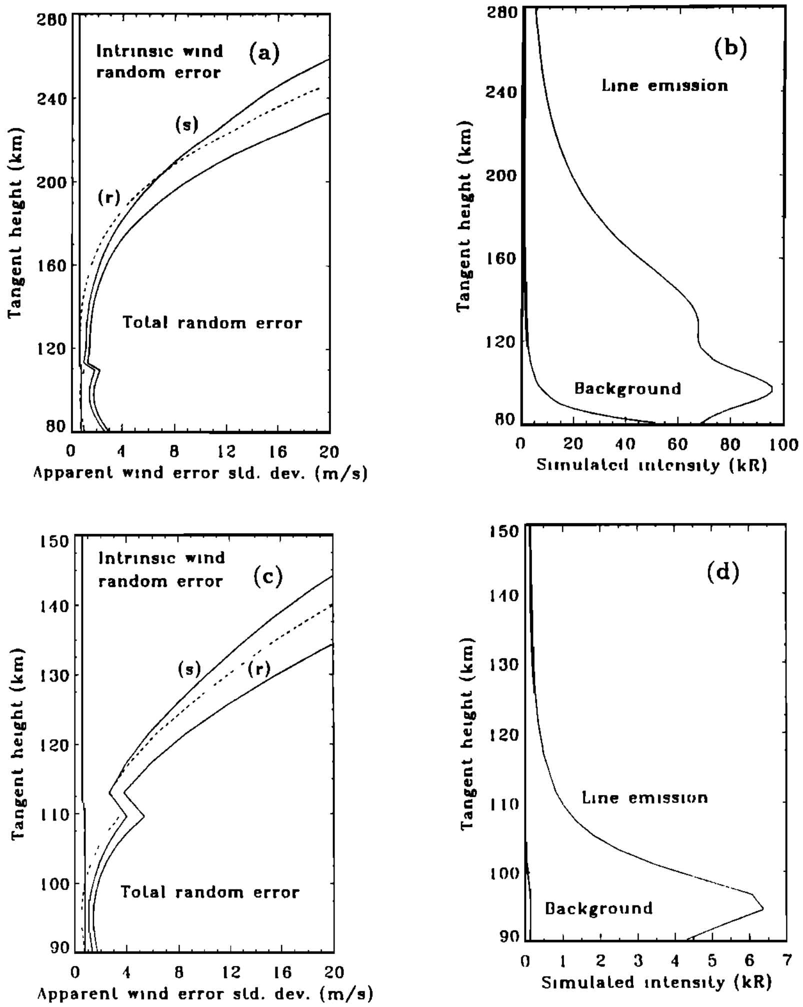

Figure 1. The apparent wind error standard deviations and associated emission rate profiles for typical (a and b) day and (c and d) night conditions. In the wind error standard deviation plots, r indicates the reading wind error and s the error associated with the shot noise.

of the form [e.g., *Twomey*, 1977; *Menke*, 1984]

$$\mathbf{x}_i = \left(\mathbf{L}_i^T \mathbf{S}_{y_{ii}}^{-1} \mathbf{L}_i + \gamma_i \mathbf{K}_i^T \mathbf{K}_i\right)^{-1} \mathbf{L}_i^T \mathbf{S}_{y_{ii}}^{-1} \mathbf{y}_i \qquad (14)$$

where

$\mathbf{x}_i$	is the solution estimate vector,
$\mathbf{y}_i$	is the data vector,
$\mathbf{L}_i$	is the limb geometry transformation matrix of the forward model $\mathbf{y}_i = \mathbf{L}_i \mathbf{x}_i$ (see Equation 21 from *Shepherd et al.* [1993]),
$\mathbf{S}_{y_{ii}}$	is the diagonal data covariance matrix,
$\mathbf{K}_i$	is the damping constraint matrix, and
γ_i	is the weighting parameter.

For the inversion, $\mathbf{S}_y$ is calculated without the contribution of the intrinsic phase random error. Each constraint matrix is a variant of a differences matrix with rows containing $[\cdots, 0, -1, 1, 0, \cdots]$ or $[\cdots, 0, -1, 2, -1, 0, \cdots]$. Relative scaling of constraint matrix rows and the value of each weight parameter are set to optimally reduce the noise in the overall profile while retaining the smaller-scale features considered significant. While work is continuing on refining the values used in the inversion process, any future adjustments are unlikely to influence the overall results presented here. A detailed account of the inversion process will appear elsewhere.

Incorporating the damping term reduces the solution random error variance estimates from

$$\sigma_{o_{ji}}^2 = \left(\mathbf{L}_i^{-1} \mathbf{S}_{y_{ii}} \mathbf{L}_i^{-T}\right)_{jj} \qquad (15)$$

to

$$\sigma_{ji}^2 = \left(\mathbf{L}_i^T \mathbf{S}_{y_{ii}}^{-1} \mathbf{L}_i + \gamma \mathbf{K}_i^T \mathbf{K}_i\right)_{jj}^{-1} \qquad (16)$$

These variances are then used to determine the final wind random error standard deviation estimates. In the calculation of these variances only the random error variance of the measurements (first term on the right-hand side of equation (11) are included in the covariance matrices $\mathbf{S}_{y_{ij}}$.

The induced error (composed of the discretization due to the finite bin size and the constraint bias), the net signal noise (standard deviations calculated using equation 15) and constrained signal noise (standard deviations calculated using equation (16) for Doppler wind

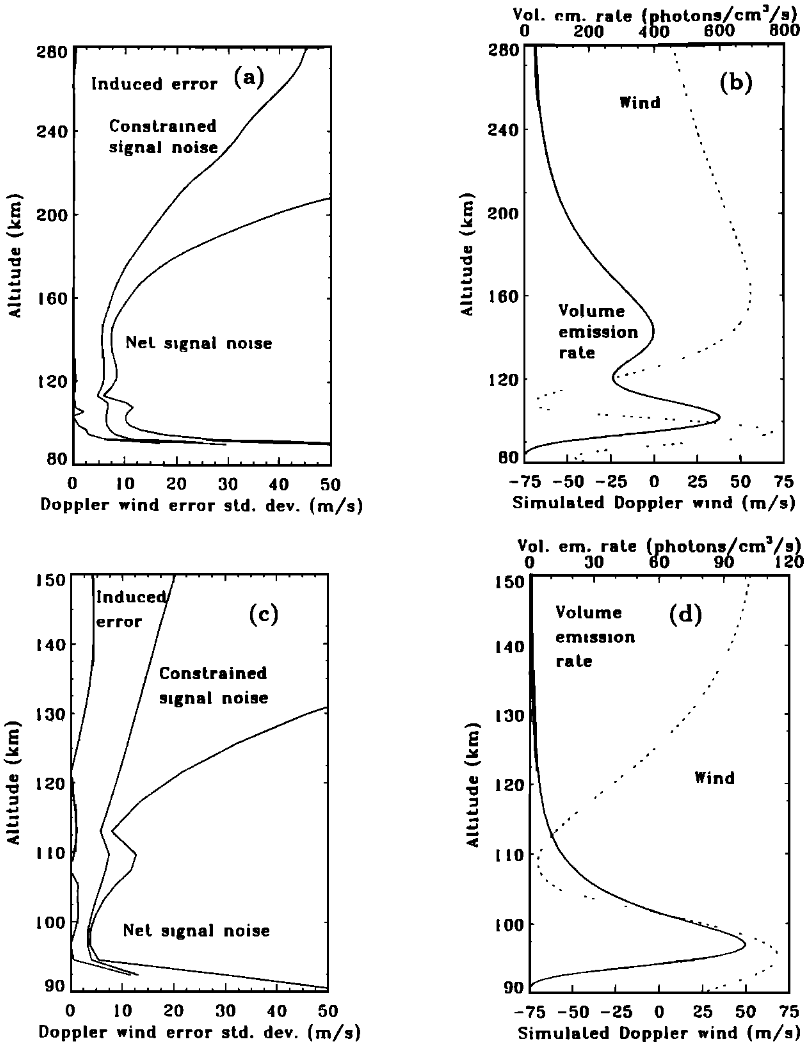

Figure 2. Typical error profiles for inverted winds and associated volume emission rate and wind profiles for (a and b) day and (c and d) night conditions.

and volume emission rate profiles typical of daytime observations (see Figure 2b), are given in Figure 2a. The corresponding nighttime profiles are shown in Figures 2c and 2d. Near the peak of the volume emission rate profile the wind standard deviation is 6 m s^{-1} for the daytime measurements and 3 m s^{-1} for the nighttime measurements. The reduction in noise associated with the use of damping in the inversions and the minimal contribution of the induced error (apart from in the region below the emission peak) is evident in these figures.

The inverted profiles are calculated for each field of view and then combined to produce zonal and meridional winds along the satellite track. These profiles are then interpolated to produce the level 3 wind fields most accessible to the scientific community. The errors provided with these data are calculated using the appropriate linear combination of the variances of the relevant profiles. The potential difference between the initial and the reduced standard deviations should be kept in mind when using WINDII winds because the standard deviations currently provided with the data are those from equation (15) as opposed to those achieved with the damping term, equation (16). The data are calculated, however, using the damping term, so that the errors provided are larger than they should be given the method of calculation. In addition, the bin bias is not subtracted from the signal in the shot noise calculations. This results in an overestimation of the random error variance of the same order as the reading error variance. These ambiguities will be resolved for data calculated using data processing software versions subsequent to version 4.23. Since each solution profile is determined independently from any other along the orbit track, further noise filtering may be achieved, when desired by the data user, through carefully weighted combinations of neighboring profiles.

4. On-Orbit characterization

4.1. Horizontal Phase Corrections

The O^1S zero reference image was produced by the two-step process described in section 2.3, but in addi-

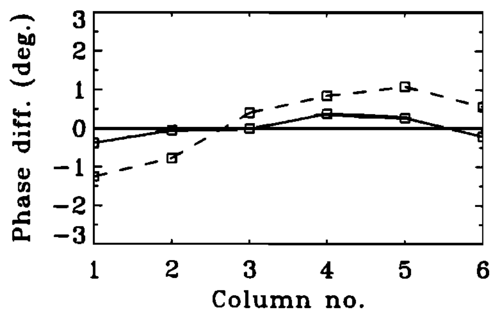

Figure 3. Typical example of lateral phase variations: O^1S, daytime bottom window of field of view 2 (FOV2), January 19, 1993. Averages for 20 rows of pixels. Dashed line shows variations before the characterization data base (CDB) adjustment, solid line after adjustment. There are six columns of bins across each field of view.

tion, the phase distribution was checked on orbit to the extent that it was possible.

It is not difficult to assess the lateral phase variations (along a row of pixels) by averaging many measurements, because the lateral variations, on the scale of the field of view, are expected to be approximately random. This was done for several days at different times in the mission by averaging the measurements for a whole day. Phase images were averaged separately for night and day apertures and for windows located in the upper and lower regions of the field of view. Measurements made near the terminator were not used. An example of the lateral variation is shown in Figure 3 (dashed line). It was generated by subtracting the row average from each value in the row, and averaging 10 such rows. It represents the phase variations that are present after correction by the zero reference phase image measured in the laboratory prior to launch. The lateral phase variations were found to be consistent for the different times sampled.

These residual lateral phase variations were averaged for several days scattered through the mission and were then used to generate images to correct the column-to-column variations in the existing zero phase reference image without changing the average values for each row. Figure 3 (solid line) shows data reprocessed using the corrected reference data. Lateral variations still exist in the data but are now about a third of the previous ones. The corrections are not expected to change the wind values obtained for each row in the image but do improve the statistics used in error estimates.

4.2. Filter Passbands

Interference filters can sometimes change their characteristics over time, so it is useful to monitor their properties during the mission. On WINDII it has been possible to study the passbands of the O^1S and O^1D filters on a regular basis using light from two of the phase calibration sources. A technique has also been developed to detect small changes in the tilt of the filters with respect to the optical axis. All the WINDII filters except for filter 5 were manufactured by Andover Corporation, who used a proprietary process to stabilize their characteristics. Filter 5 (the broad-band OH filter) was provided by Barr Associates.

The data used for the analysis come from the weekly major calibrations. In particular, absolute transmittance images of the filters taken with the night aperture are obtained at the wavelengths of the Kr (557.0 nm) and Ne (630.4 nm) calibration lamps. The data used here are from a period beginning shortly after launch and ending in December 1993. These data are com-

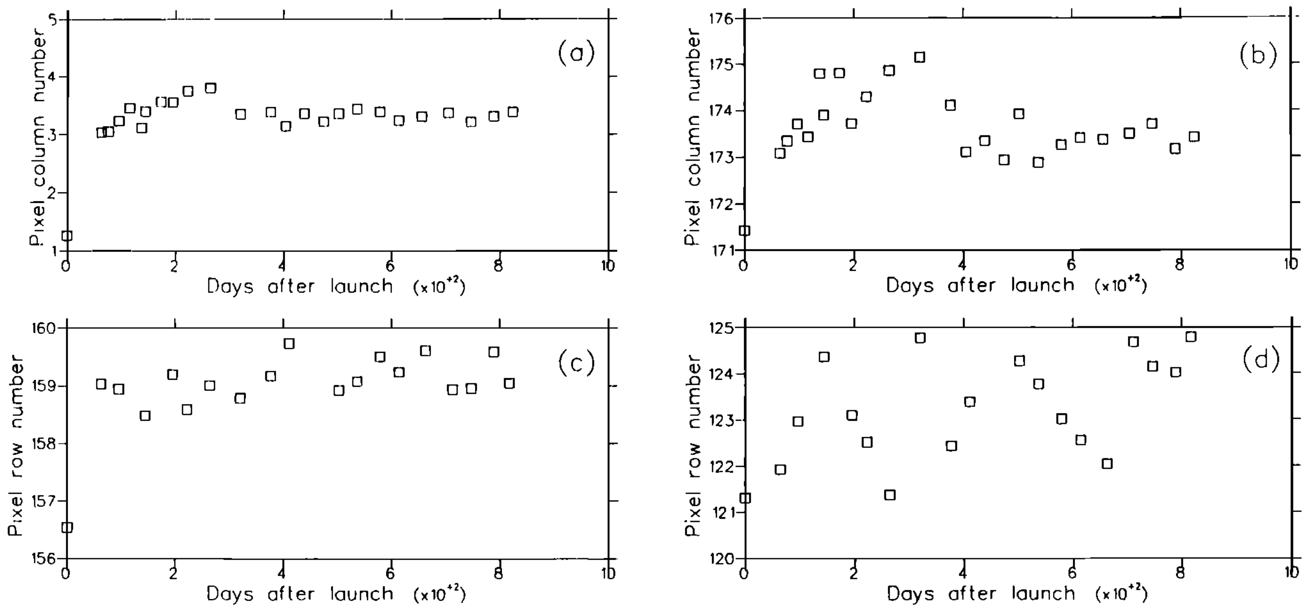

Figure 4. Locations of the normals for the O^1S and O^1D filters as functions of mission time. (a and b) Horizontal and vertical coordinates for the O^1S normal (located in FOV1). The prelaunch values are at day zero. (c and d) Same for the O^1D filter (in FOV2).

pared with similar transmittance images obtained before launch.

The transmittance images are circularly symmetric and the center of the pattern marks the direction of the normal to the filter. A convenient way to study the changes in the tilt of the filters is to plot the location of the center of the transmission pattern as a function of time. For this purpose the centers of a selected number of rings of constant transmittance were computed, and a weighted average of these centers was taken to be the estimated direction of the filter normal. Figure 4 shows the horizontal and vertical locations of the estimated centres for the O^1S and O^1D filters on the CCD for a selected number of calibrations taken between launch and the end of 1993. It can be seen from the plots that there has been no significant drift in the tilts of the two filters since launch, although a slight shift of the order of 3 to 4 pixels in the horizontal direction toward the outer edge of FOV1 can be observed between the ground (day zero) and flight positions for both filters. The CDB has been adjusted for the effect of this small shift in the filter axis and no significant effect on the measurements is expected.

In examining the transmittance of the filters at the wavelengths of the calibration lamps, advantage was taken of the inherent circular symmetry of the transmittance images around the filter normal. The average transmittance was computed for each image as a function of angular distance from the filter normal. Figures 5a and 5c show typical plots of the averaged transmittance against angular distance from the estimated filter normals. The averaged transmittance at a selected number of incident angles was then plotted as a function of time. Figures 5b and 5d show variations in the averaged transmittance at fixed angles from launch to the end of 1993 for the O^1S and O^1D filters respectively. The shift between the ground (day zero) and flight is about -0.05 nm for both filters, and is likely due to a temperature difference. Since then the O^1S filter has shown no long-term drift exceeding ±0.01 nm and the O^1D filter has apparently drifted back +0.03 nm, or 1% of its bandwidth, during the time in orbit. These filters can therefore be considered essentially stable.

Finally, although the transmittance of the two filters was studied using only the WINDII night aperture, it is reasonable to assume that similar results hold also for the day aperture, which uses approximately 11% of the area of the filter lying within the area used by the night aperture.

4.3. Responsivity

The tungsten halogen lamp is observed through each filter about once a week during the major calibrations as a partial check on the instrument's responsivity. Figure 6a shows the normalized response curves for filters 1 to 6. The response to the tungsten lamp has decreased by 3 to 7% over 1100 days, with the most rapid change near the beginning, and leveling off after day 800. This could be understood as a change of temperature of the tungsten lamp combined with darkening of the envelope, affecting the shorter wavelengths (filters 1, 2 and 3) more than the longer ones. Other possibilities are radiation darkening of glass elements, changes in the integrated filter transmittance, and changes in the CCD, in which case the instrument's responsivity could be affected. As section 4.2 showed, filters 2 and 3 appear to

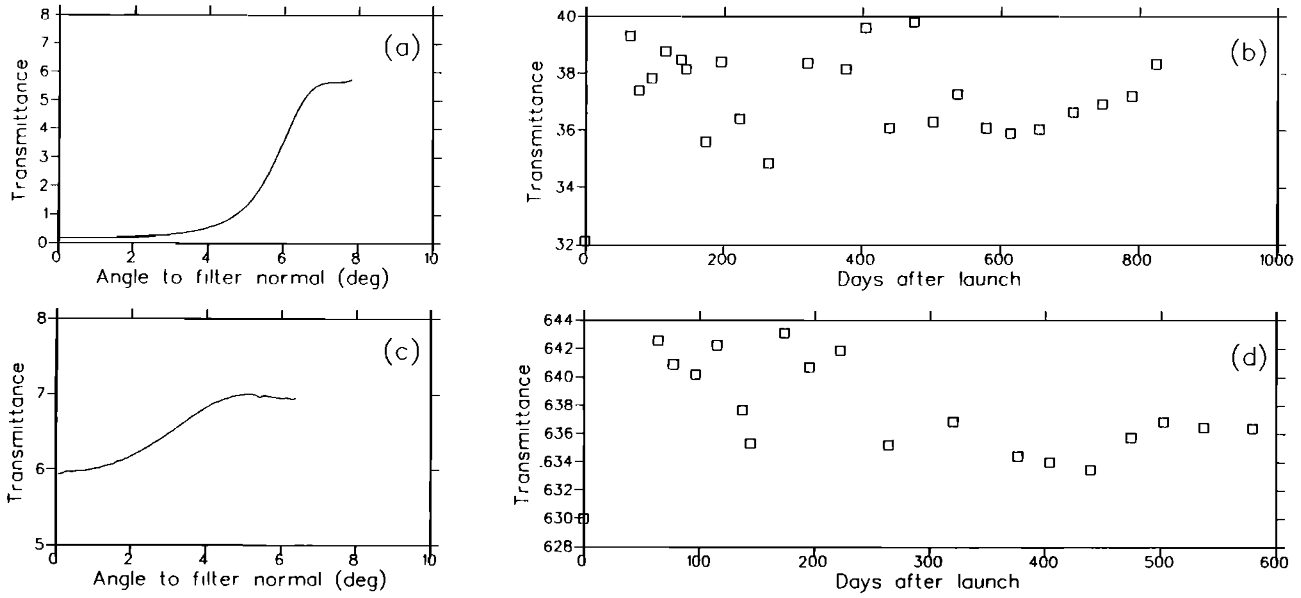

Figure 5. (a) Typical average transmittance as a function of angle from the O^1S filter normal. (b) The same for the O^1D filter. (c) Average transmittance 6° from the O^1S filter normal as a function of mission time. The prelaunch value is at day zero. (d) The same for the O^1D filter at 3° from the normal.

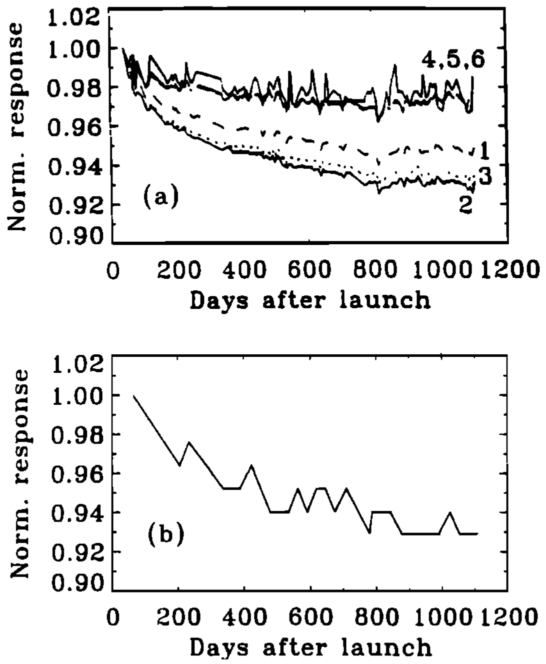

Figure 6. (a) CCD response to the tungsten calibration lamp as a function of mission time. Each curve represents a different filter and is normalized to the initial point. The wavelengths for filters 1, 2, and 3 are, respectively, 553 nm (background), 558 nm (O^1S), and 630 nm (O^1D). filters 4, 5, and 6 are the OH group, 730–735 nm. Data for filter 7 (O_2 at 763 nm) are not plotted but are very similar to the OH group. (b) Normalized response of the lamp's photodiode monitor for the same period. The wavelength is 540 nm. The discrete levels are caused by coarse digitizaion. Data are not available for every calibration.

be very stable, so the effect is not likely due to them. Furthermore, Figure 6b shows that the change in signal from the tungsten lamp's monitor is about the same as for filters 2 and 3. The monitor is a filtered photodiode placed near the lamp with no intervening optics and records the lamp output at 540 nm (bandwidth is equal to 9 nm). Since the lamp is the one element common to the measurements with the CCD and the monitor, it is reasonable to suppose that the observed changes have occurred in the lamp. Therefore no adjustments have been made to the responsivity in the database. One curious feature of Figure 6a is that filter 1 seems out of place, being less affected by the changes than filters 2 or 3, which are at longer wavelengths.

4.4. Long-Term Phase Drift

In addition to the expected small variations in phase due to thermal variations, a longer-term drift in the Michelson phase is observed which cannot be related to temperature. This drift was tracked using the weekly phase calibrations and is illustrated in Figure 7a for the four emission line sources on WINDII, represented in the figure as E1 (Kr 557.0 nm), E2 (Ne 630.5 nm), E3 (Ar 738.4 nm), and E4 (Ar 763.5 nm). Data are shown for the first 810 days of flight, during which the phase changed by 450° to 600°, depending on the wavelength. The variation has the form of a relaxation process with a timescale of about 225 days. The cause of the phase drift is not known but could be due to changes in the glass, the glue layers or dielectric coatings on the surfaces, or a relaxation of the clamping pressure on the interferometer. Gaps in the data correspond to times when the UARS instruments were turned off. The sudden jumps in phase occur at resets, when the instrument is powered on after having been turned off for some reason, and the mirror alignment returns to a slightly different setting. For each of these segments a new characterization database was constructed using calibration data to account for the effect of these variations in phase. These changes have not had an adverse effect on the Michelson's ability to modulate emission lines. The visibility of the laser source, measured during major calibrations, has remained above 0.9 throughout the mission.

As mentioned in section 1, zero wind calibrations were made on the ground prior to launch and are assumed to be valid after launch. This assumption cannot be checked directly from the phase calibrations of individual lines because of the possibility of changes occurring in the interferometer during launch which might cause phase wraparounds. This may, however, be checked by considering the phase difference between calibrations at different wavelengths. This phase difference is a slowly varying function of path difference and thus is much less susceptable to ambiguities than the phase of a single line.

The variations of phase differences (E1-E2) and (E3-E4) have been converted to changes in path difference (assuming no dispersion) and are plotted in Figure 7b. The agreement between the two curves is excellent and indicates that the assumption of no wraparound is correct. The phase difference on orbit matches that on the ground at day 151 for both cases. This date is indicated by the vertical line in Figure 7a. The ground phase difference does not match the phase difference on orbit at day 0 because of the change in medium (air to vacuum) in the interferometer gap between ground and orbit.

The results of this calculation indicate that the Michelson interferometer has been extremely stable with the stresses of launch causing changes in the path difference of ~ 50 nm. Such changes are minimal and provide justification for the initial use of the ground calibration data in orbit.

The gradual phase drift described here also implies a drift in the zero reference because the phase calibrations and atmospheric measurements are made at different wavelengths. In the case of O^1S the wavelength difference is 0.7 nm, causing an effective shift of 9.5 m s^{-1} in the zero reference due to the observed increase of 600° of phase (1.67 orders of interference) in the first 800 days of the mission. This effect is corrected in the reduction of the data.

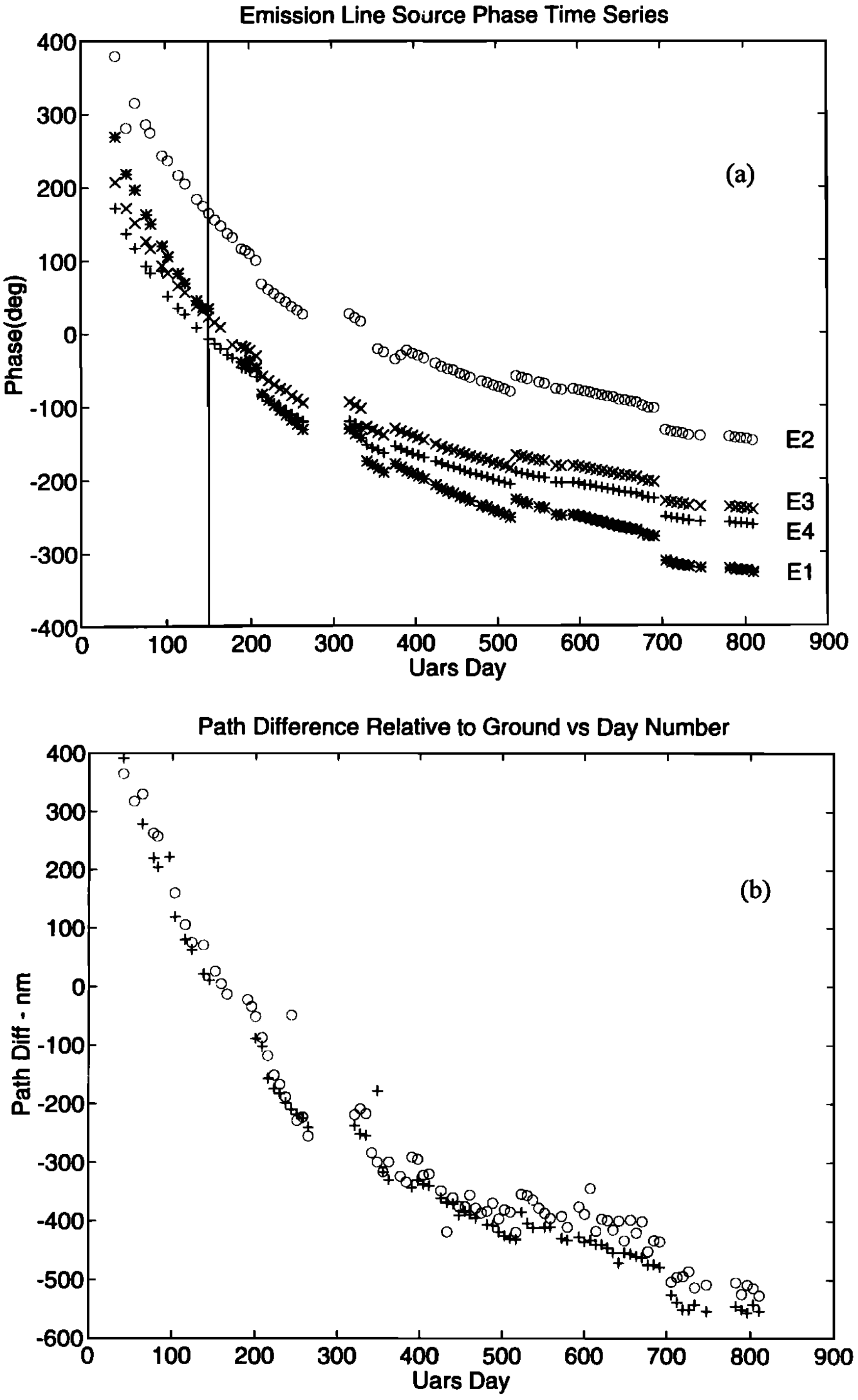

Figure 7. Long-term phase variation. (a) Phase as a function of mission time for the four calibration sources, E1 to E4. (b) Path difference relative to prelaunch values, calculated from E1 to E2 and E3 to E4.

4.5. Limb Heights in the WINDII Images

The tangent limb altitudes for the image elements in each WINDII field of view were computed using UARS orbital information combined with a knowledge of the relative orientation of WINDII with respect to the spacecraft. The approximate orientation was determined before launch, but more precise on-orbit values were obtained using weekly sequences of WINDII star images.

Because of the requirement for precise absolute limb heights, redundant methods were employed to evaluate the transformation matrix relating the spacecraft frame of reference to the WINDII instrument pointing frame for each field of view. The matrix elements were determined by referencing the absolute WINDII inertial

Table 1. Differences Between Limb Heights (km) Computed by Two Independent Methods Using WINDII Star Images

UARS	Number of	Avg.Ht.Diff./s.d.			
		FOV1		FOV2	
Yaw	Yaw Periods	Column 1	Column 6	Column 1	Column 6
Forward	4	0.58	0.23	0.33	1.03
		0.39	0.64	0.34	0.60
Reverse	4	0.80	0.10	-0.15	0.85
		0.70	0.50	0.26	0.30

orientation, as determined from measurements of star locations in each field of view, to the coincident absolute orientation of the UARS frame of reference. The average limb heights determined with the redundant methods differed by about 0.5 km (Table 1).

Ideally, the transformation matrix for each yaw orientation should be constant with time, but in practice there are slight variations. For example, any error in the absolute orientation of the UARS frame of reference will result in a fundamental limitation in the determination of the pointing accuracy of the WINDII fields. The magnitude of this variation was estimated by taking a sequence of star images over a short period of a few minutes, during which time the spacecraft thermal environment was not rapidly changing, and evaluating the relative pointing between the UARS frame and the WINDII frame for each image. The variation in vertical limb height component, which corresponds approximately to the spacecraft roll component, arising from the relative "drift" between the two frames (Figure 8) had a standard deviation of about 0.4 km. This is equivalent to about 0.6 arc minutes which is approaching the pointing stability of the spacecraft.

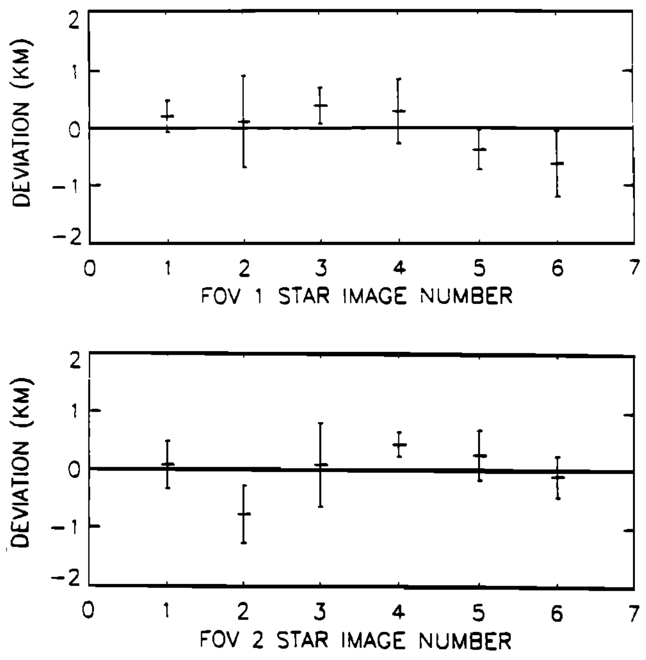

Figure 8. An example of the variations, expressed as limb tangent height deviations, inherent in the transformation matrix from the UARS frame of reference to the wind imaging inferometer (WINDII) instrument pointing frame. The data are from a sequence of six individual star images taken over an observing period of 11 min on September 19, 1994. Approximately four such sequences are recorded in each yaw period to provide data for the updated matrix for that period.

The corresponding drift in spacecraft yaw, which will introduce errors into the determination of wind velocities, relative to the yaw component determined from the WINDII star images was found to be about 0.5 arc min. This corresponds to a wind error of less than 1 m s^{-1}. For spacecraft pitch, by comparing the simultaneous offsets in star locations in the two fields the drift between the two reference frames was determined to be about 0.8 arc min.

In addition, an estimate of the total error in pitch can be made by observing the relative height constancy of the peak of the hydroxyl airglow layer from field to field. Data for this comparison were carefully selected to minimize the effects of true layer height variations by limiting the comparison regions to narrow latitude bands and also by comparing the fields from opposite yaw periods to further check for possible systematic differences. A data set of 24 images was selected from five consecutive orbits on March 22,1992, and 23 images from March 27,1992. The average difference in peak height between the two fields was about 0.5 km (Table 2) which corresponds to a spacecraft pitch error of about 1 arc min.

In summary, the validation results indicate that the pointing error in the tangent limb altitudes is less than 1 km and in the winds is less than 1 m s^{-1}.

5. Wind Comparisons With Ground-Based Instruments

Comparisons have been made between winds measured by WINDII and by optical interferometers and

Table 2. OH Layer Heights From Line-of-Sight Images

Date	UARS Yaw	FOV	Lat °N	Peak (km) /s.d.	Column Offset (km)/s.d. (km) 1	2	3	4	5	6
March 22, 1992	Reverse	1	10-30	86.16	0.05	-0.02	-0.06	-0.04	-0.05	0.12
				1.25	0.23	0.18	0.11	0.12	0.13	0.16
		2	35-55	86.83	0.26	0.04	0.04	-0.15	-0.11	-0.08
				0.98	0.31	0.24	0.20	0.16	0.31	0.33
March 27, 1992	Forward	1	30-40	86.24	0.19	0.00	0.04	-0.05	-0.10	-0.08
				0.40	0.19	0.13	0.25	0.39	0.17	0.19
		2	10-25	85.63	0.05	0.06	0.07	-0.02	-0.18	0.02
				1.68	0.19	0.16	0.12	0.23	0.28	0.28

radars at several ground stations in an attempt to verify the zero reference used by WINDII. The ground-based instruments include a Michelson interferometer (MICADO) at the Observatoire de Haute-Provence (OHP); Fabry-Perot interferometers at Mount John and Peach Mountain; MF radars at Adelaide, Christmas Island, Saskatoon, and Urbana; and the EISCAT incoherent radar facility. The data reported here are mostly direct comparisons, in which the wind measured by the ground instrument is compared with the wind measured by WINDII at the time that the WINDII field of view passed close to the ground station.

In spite of efforts to compare measurements as directly as possible, the different geometries of the satellite and ground-based instruments preclude an exact comparison. This is illustrated by the scale drawing in Figure 9. WINDII integrates the signal over approximately 600 km along the line of sight and laterally about half that distance due to the width of the field of view and the motion of the spacecraft during the measurement. The ground-based interferometers sample the airglow layer at four points 160 km from the station, and the MF radars sample a cone with a diameter of 50–100 km at the height of the layer above the station. The timing is also different, as WINDII completes a measurement in 10–20 s while the ground data have been integrated longer, up to 1 hour for some of the radars. In addition, it is very rarely that the region sampled by WINDII is centered exactly over the ground station, as suggested in Figure 9. The ground range from the station to the midpoint of the sampled region is therefore a parameter in the selection of data for comparison. Because the work has been carried out independently by several different groups, the selection criteria are not the same for all data sets. Local variations, such as those caused by gravity waves [e.g.,

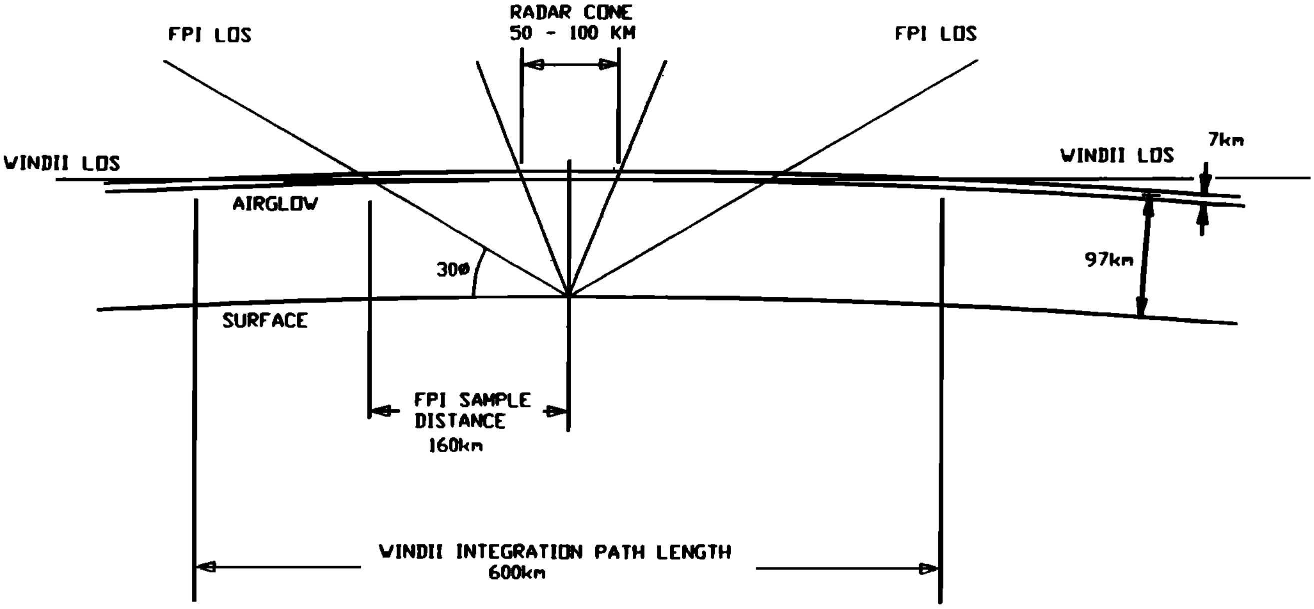

Figure 9. Geometries of WINDII, ground-based interferometers and MF radar observations, drawn to scale. WINDII integrates over a path length of 600 km for a typical layer thickness of 7 km. The interferometers take much smaller but widely spaced samples. (LOS, line of sight)

Taylor et al., 1987], are bound to cause differences between WINDII and winds measured from the ground, but since the local conditions are expected to be random over the long term, the averaging of many comparisons should lead to agreement. If this wer not so, then the whole procedure of upper atmosphere wind measurement would be in question.

The comparison data sets all show large scatter, no doubt in large part due to the reasons mentioned above. The number of good comparisons is limited not only by the UARS orbit but also by operational factors such as the weather at the optical ground stations. One might wish for more data points for each station, but it is the combined results from all the stations which must be considered in evaluating the significance of the wind validation. The results from the different ground stations are described in the following sections. Conclusions are summarized in section 8.

5.1. MICADO Measurements at the Observatoire de Haute-Provence

The MICADO instrument (Michelson interferometer for coordinated auroral doppler observations) consists of a field compensated Michelson interferometer [*Bouchareine and Connes,* 1963] thermally stabilized to allow wind and temperature measurements [*Thuillier and Hersé,* 1991]. It is located at the Observatoire de Haute-Provence (OHP); 44°N, 6°E) and was selected as a collaborative experiment for WINDII. Observations began at OHP throughout in October 1991 and are continuing. Previously, MICADO was used in three campaigns in the northern auroral zone [*Thuillier et al.*, 1990; *Lilensten et al.*, 1992; *Fauliot et al.*, 1993]. The results of the MICADO-WINDII comparisons are summarized here. More details are given in the accompanying paper [*Thuillier, et al.*, this issue].

The MICADO and WINDII interferometers have a similar principle of design and measurement [*Thuillier and Shepherd,* 1985]. For MICADO a movable telescope allows observations at the zenith and in other directions in order to derive horizontal and vertical winds. The accuracy of the measurements for typical emission rates at midlatitudes is about 5 m s^{-1}.

O^1S emits in both the E and the F regions and a ground-based interferometer measures the integrated signal from both regions. At midlatitudes the E-region emission rate is usually much greater than for the F region, as is shown by WINDII. Nevertheless, the wind measured by a ground-based instrument can be affected by the F-region contribution, for which the winds are generally much greater than near the mesopause. It appears difficult to eliminate certain measurements having a potential F-region contribution, such as after sunset. The wind measured by a ground-based interferometer is the result of an integration through the entire emitting region. These data cannot be inverted, so in order to compare with the wind measured from orbit, a numerical integration is made for the geometry of the MICADO measurement, through the layer as observed by WINDII. Details of this procedure are given by *Thuillier, et al.* [this issue].

MICADO made observations (1) extending one hour one each side of a satellite overpass, providing sometimes two or three passes per day, and (2) a minimum of one complete night for each month in order to observe seasonal and diurnal wind variations. In both cases the zonal and the meridional wind components are measured as a function of time and interpolated at the local time of the WINDII pass. The area for correlated measurements between the two instruments is defined within (40°N - 48°N) and (10°W - 20°E) in longitude. Passes which occurred within this window were further selected according to local weather conditions, quality of the WINDII data, local time, and homogeneity of the local wind field as measured by MICADO. Homogeneity is determined by comparing the wind measured in two opposite directions. This careful selection eliminates about 80% of possible correlations.

Observations made from October 1991 to April 1994 were used to study the semidiurnal tides at midlatitudes as a function of season [*Fauliot et al.*, 1994]. They agree with the major characteristics of E-region circulation at midlatitudes determined from radar measurements [*Manson et al.*, 1989; *Massebeuf et al.*, 1981] as well as with the theoretical predictions by *Forbes and Vial* [1989].

As the direct comparisons were distributed approximately evenly throughout the $2\frac{1}{2}$ year period of observations, it was possible to look for a trend in the WINDII zero reference. A straight line was fitted to the WINDII–MICADO differences as a function of time, but no significant trend was found [*Thuillier, et al.*, this issue].

While MICADO data are processed up to the date of writing, the period considered in this study extends from the end of December 1991 to the end of January 1994 due to the availability of the WINDII data at the time of this analysis. Because of several factors, including orbital geometry and the weather at the ground site, this period yielded only 34 direct comparisons, corresponding to 21 days. Most of the correlations occurred when WINDII was looking southward. The small number of effective direct comparisons led us to consider three kinds of correlations:

(1) direct correlations: WINDII observations are made at the same local time and day as the MICADO measurements; (2) correlations within 1-5 days: WINDII observations are made at the same local time but within 1-5 days with respect to MICADO observations; (3) monthly correlations: for each month, WINDII and MICADO data are organized as a function of time in 1-hour bins.

The WINDII data used in this study were processed with version 4.23 of the production software, which provides zonal and meridional wind components. Figures 10a and 10b show the results of the direct corre-

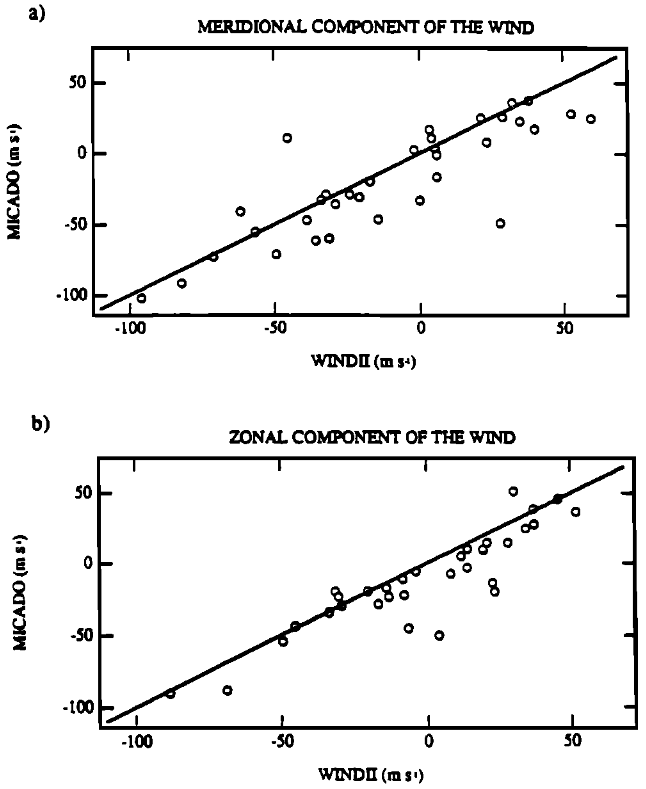

Figure 10. Relationship between the wind measured by the Michelson interferometer for coordinated auroral Doppler observations (MICADO) and WINDII in the vicinity of the Observatoire de Haute-Provence (OHP) for the direct correlation cases. (a) Meridional component, (b) zonal component.

lations as scatterplots, one for each component. The points lie close to the bisector. We note that the velocity range of these correlations extends from -100 to 50 m s^{-1}. For both components the mean WINDII - MICADO differences and the corresponding standard deviations are given in Table 3. They are relatively close to one another, around 10 m s^{-1} and 20 m s^{-1}, respectively.

Within 1-5 days between the WINDII and the MICADO measurements the yield of effective correlations increases to 70. The results are shown in Table 3 and are consistent with the previous results. An increase of the standard deviation is noticeable due to the natural day-to-day wind variability which has been observed to be 15 m s^{-1}. The meridional standard deviations are larger than the zonal ones for both the direct and the 5-day measurements and the difference is the same in both cases.

For each month of the year, MICADO data and WINDII observations near the observatory were organized as a function of local time and averaged over 1-hour boxes. Then, the difference between the resulting monthly mean local time variations of the wind of both experiments are calculated. The comparison is extended over the year by averaging those differences. The results are included in Table 3 in columns 6 and 7. The meridional and zonal standard deviations and the difference between them are reduced in the case of the monthly averages, possibly as a result of the method of averaging.

A given offset in one field of view will affect the calculated meridional and zonal wind components differently according to the particular geometrical conditions of viewing. This is why, knowing the difference between MICADO and WINDII for each component and knowing the line-of-sight angles used in the vectorial recombination, we have calculated the corresponding difference per field of view and their mean value. This calculation has been carried out for the direct correlations only. As listed in Table 4, the WINDII-MICADO differences are almost the same for the two fields of view, 9.2 and 8.9 ms^{-1} for FOV1 and FOV2, respectively. The significance of this is discussed in section 8, where all the results are compared.

5.2. FPI Measurements at Peach Mountain and Mount John

Two ground-based Fabry-Perot interferometer (FPI) installations have provided green line wind measurements for WINDII comparison. The Peach Mountain Observatory (42.4°N, 83.9°W), operated by the University of Michigan, produced 15 nights of data coincident with WINDII overflights since June 1993. The station at Mount John, New Zealand (44.0°S, 170.5°E), operated by the Universities of Washington and Canterbury gave 22 nights on which WINDII and the FPI measurements overlapped during 1992 and 1993. In both of these ground-based installations the FPI measures in the four cardinal directions at an elevation angle of 30° and records zonal and meridional winds every quarter hour.

Table 3. Mean Values and Standard Deviations of the WINDII-MICADO Differences for Direct, 1-to-5-Day and Monthly Correlations

	Direct		± 5 days		Monthly	
Component	Meridional	Zonal	Meridional	Zonal	Meridional	Zonal
Mean, m s^{-1}	9.0	9.9	11.8	8.9	12.4	10.1
s.d., m s^{-1}	21.1	15.1	31.8	25.9	23.8	21.7

Table 4. Mean Values and Standard Deviations of the WINDII-MICADO Differences for the Two WINDII Fields of View, Using Direct Correlations

	FOV1	FOV2
Mean, m s^{-1}	9.2	8.9
s.d., m s^{-1}	23.9	20.8

To compare these ground-based FPI measurements with the WINDII line-of-sight inverted winds, the two orthogonal FPI wind components were added vectorially along the WINDII field-of-view direction. As with MICADO, the ground-based FPI sees only the integrated wind from the emission region, and because the inverted data from WINDII give the wind as a function of height, it is necessary to compute a single weighted mean wind for each comparison with the FPI measurements. The weighting function was the volume emission rate, computed for each altitude element from the same WINDII measurement used to calculate the wind profile. All possible WINDII wind profiles were used in this way as long as the tangent point at the altitude of maximum volume emission rate lay within a maximum ground range of 1000 km of the station. By this method, three or four profiles were used as one field of view swept over the station field, and the same FPI readings modified by the changing WINDII direction were used for all. Multiple passes gave comparison data for Peach Mountain but not for Mount John.

The results of the FPI comparisons are shown by the scatterplots in Figure 11 and the important results of these comparisons are summarized in Table 5. The mean differences are listed separately for the two WINDII fields of view, where equal statistical weight was given to every pass. For both FPI instruments the mean differences are less than the WINDII design goal of ± 10 m s^{-1}. The standard deviation of the differences, with an average of 25 m s^{-1} for the two stations, is somewhat larger for Peach Mountain than for Mount John, which confirms the visual impression given by the scatter plots. The scatter, of course, includes noise components in both the WINDII and the FPI measurements, as well as geophysical effects. Both FPI sites found similar differences between the two fields of view, about 9 m s^{-1} for ΔFOV1-ΔFOV2.

5.3. Comparisons With EISCAT Radar Measurements

EISCAT coordinated experiments have been used to derive the neutral wind at 100 km and 170 km altitudes during WINDII passes over Scandinavia. Because of the very high latitude of the EISCAT facility (Tromsø, 69.6°N), WINDII overpasses occur mainly during daytime. This is because WINDII is on the cold side of the spacecraft, looking away from the Sun, and can only see the latitude of Tromsø at the top of its orbit. We use here four days in May and August 1992, chosen for their low magnetic activity. For each day, there are two successive passes with a ground range from Tromsø of less than 300 km. The incoherent scatter technique provides measurements of the ion density, temperature, and velocity, with an altitude resolution and a time integration that depend on the experimental configuration. At E-region heights the frequency of collisions between ions and neutrals is large enough that the ion velocity and neutral wind are essentially the same. Tristatic measurements of the ion velocity at an altitude close to 100 km were used to deduce the meridional and zonal component of the neutral wind. The altitude resolution of the tristatic measurement is determined by the intersection of the emission and reception beams, about 1 km. At F-region heights, only the meridional component of the neutral wind can be deduced using the ion velocity along the magnetic field. We make the comparison at 170 km altitude where the ambipolar diffusion

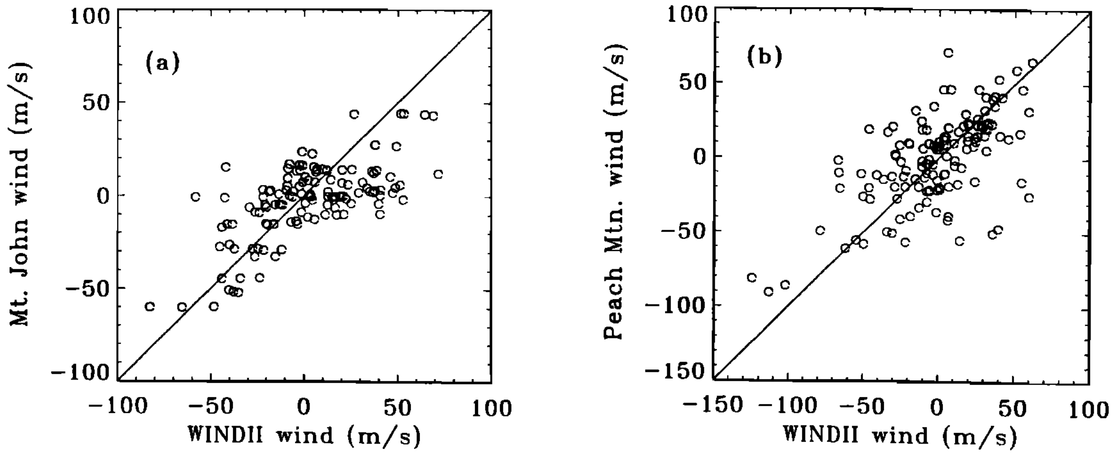

Figure 11. Scatter diagrams for comparisons with Fabry Perot interferometer measurements: (a) Mount John, 1992-1993. (b) Peach Mountain, 1993-1994. Data from FOV1 and FOV2 are plotted together in these diagrams.

Table 5. Summary of FPI Comparisons

Quantity	Mount John	Peach Mountain
Number of passes FOV1	20	30
Mean difference (WINDII - FPI) = ΔFOV1	+8.1 m s^{-1}	+4.0 m s^{-1}
Number of passes FOV2	19	27
Mean difference (WINDII - FPI) = ΔFOV2	-0.4 m s^{-1}	-5.8 m s^{-1}
Offset, ΔFOV1 - ΔFOV2	8.5 m s^{-1}	9.8 m s^{-1}
s.d. of ΔFOV	21.7 m s^{-1}	28.1 m s^{-1}

velocity of the ions is negligible. Therefore the ion velocity along the magnetic field is the projection of the meridional component of the neutral wind. We use here a monostatic measurement, which means that the altitude resolution is given by the length of the pulse emitted. It corresponds in our case to about 40 km. The comparison is done on the basis of individual WINDII and EISCAT vertical profiles, using for the latter an integration time of 5 min for May 12, 16, and 19, 1992, and 1 min for August 1, 1992. WINDII winds obtained with software version 4.23, after recombination of the two fields of view, have been interpolated at the altitude of the EISCAT measurement in the E region. In the F region, because of the large altitude resolution of the EISCAT measurement which is centered at 168.5 km, no interpolation has been done. Figure 12 shows a scatterplot of the two components of the EISCAT and WINDII winds at 100 km altitude (Figures 12a and 12c) and of the meridional component at 170 km (Figure 12b). One can see that the scatter is small around the unit slope line (indicated on the figure by the solid line) for the meridional wind at both altitudes. The scatter is larger for the zonal wind. The mean differences and their standard deviations are given in Table 6. The standard deviation of the differences of the zonal winds is the largest. The correlation coefficients are high for the meridional component, respectively, 0.81 and 0.83 at E and F region heights, and only 0.41 for the zonal component, confirming the visual impression given by the scatterplots. We have not found any explanation of this difference of behavior is not because one of the WINDII fields of view dominates in the calculation of a given component, as WINDII measurements above Tromsø correspond to the top of the orbit, so the fields of view contribute approximately equally. Considering the different measurement techniques used for the determination of the winds and the small number of points used in this statistical comparison, the agreement found is remarkably good.

5.4. Comparisons With MF Radar Measurments

Comparisons have been made between winds measured by WINDII and those obtained during WINDII passes in 1992 and 1993 at several ground-based MF radar stations. The radar winds were provided as vectors but, for the purposes of this comparison, were resolved into components along the directions of WINDII's two fields of view, and the comparisons done for each field of view separately. The WINDII winds have been inverted, so give profiles of the wind as a function of height. Passes were not used if the ground range from the station to the region observed by WINDII exceeded 500 km. The radar winds used in these comparisons have been averaged for half an hour to one hour, centered on the time of the WINDII pass. The intent of the temporal averaging is to remove small-scale features in a way that simulates the spatial averaging of WINDII. The radar stations and numbers of compar-

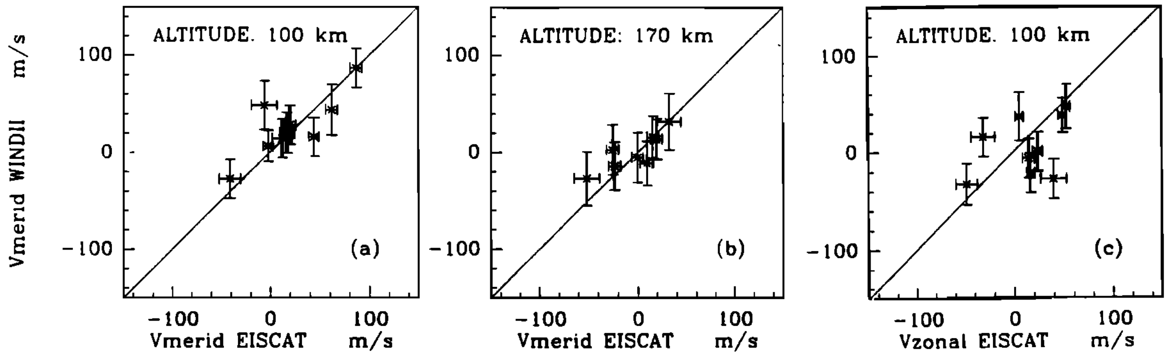

Figure 12. Scatterplots for WINDII – European incoherent-scatter (EISCAT) radar comparisons. (a and b) Meridional components at 100 and 170 km, respectively. (c) Zonal component at 100 km.

Table 6. Summary of EISCAT Comparisons

Wind Component	Altitude km	Number of Passes	Mean Wind Differences (WINDII–EISCAT), m s^{-1}	s.d. of difference, m s^{-1}	Correlation Coefficient
Meridional	100	9	4.7	23	0.81
Meridional	170	8	3.5	16	0.83
Zonal	100	9	-9.0	35	0.41

isons used from each are given in Table 7. The numbers are weighted about 3:1 in favor of daytime comparisons.

Figure 13 shows the average difference for each station between the wind measured by WINDII during the overpass and that measured by the radar in a period centered on the time of the overpass. These are given separately for the two fields of view as a function of height. The standard deviations for these averages are large, in the range 40 to 60 m s^{-1}, indicating that there is a large scatter in the individual comparisons. The overall means for the four curves are shown as solid lines in the figure.

In FOV1 the agreement with WINDII is excellent at the bottom end of the curves, near 88 km. The overall mean difference increases but remains between 10 and 15 m s^{-1} from 90 to 100 km. In FOV2 the mean is between +5 and -5 m s^{-1} in the same height range. Figure 14 shows a scatterplot for comparisons made at Adelaide between 92 and 94 km altitude. The points do not lie along the diagonal and illustrate the general tendency for WINDII to see stronger winds than the radar. The reason for this is not yet understood. It may indicate that the temporal averaging that was done for the radar data, or averaging that is inherent in the method itself, is not equivalent to the spatial averaging of WINDII, or it may indicate a more fundamental problem. In this connection, we note that the spread in the WINDII-RADAR differences increases with increasing altitude. Figure 13 shows that the agreement is best at altitudes of 88-90 km. The study of these effects is continuing and will be the subject of a future paper.

Table 7. MF Radar Stations

Station	Coordinates	Number of Comparisons FOV1	Number of Comparisons FOV2
Adelaide	35°S, 138°E	83	67
Christmas Island	2°N, 158°W	45	39
Saskatoon	52°N, 106°W	33	27
Urbana	40°N, 88°W	15	15

6. Comparisons With HRDI

The high resolution doppler imager (HRDI) [*Hays et al.*, 1993] is the other instrument on UARS that measures horizontal winds. HRDI makes daytime measurements, using the O_2 (0,0) atmospheric band, that extend from approximately 50 to 115 km and nighttime measurements at the apparent maximum of the same emission at approximately 94 km. Unlike the daytime winds, however, the nighttime data are not inverted. HRDI also measures stratospheric winds in the daytime.

HRDI uses a technique called sequential estimation to remove excessive noise in the daytime wind measurements that is generated by the inversion process. This process smooths the resulting wind fields somewhat in the horizontal, in contrast to WINDII, where each profile is inverted separately. Since smaller-scale geophysical signals, such as gravity waves, will be smoothed out by this process, one would expect some discrepency between individual WINDII and HRDI measurements. The best agreement between the two instruments should then occur after some form of horizontal averaging has been applied to both data sets.

Zonal averaging of many days of data is a simple means of determining possible systematic differences between the two instruments. This method, which was employed by *McLandress et al.* [1994] to isolate the tidal components of the green line winds, entails first separating each day of data into upleg (ascending) and downleg (descending) orbital tracks, binning in 5° latitude increments, and then averaging over longitude. In the present analysis, consistent and directly comparable data sets for both WINDII and HRDI are obtained by zonally averaging many days of data and examining the mean differences. This "matching" data set consists of 91 days of wind data extending from February 12, 1992, to February 3, 1994, and comprises only days when both WINDII and HRDI were simultaneously making daytime lower-thermospheric measurements. Since WINDII always measures on the cold side (i.e., the antisunward side) of the spacecraft, all warm side HRDI measurements are excluded from this analysis. Consequently, the resulting multiday WINDII and HRDI data sets contain nearly identical local time coverage.

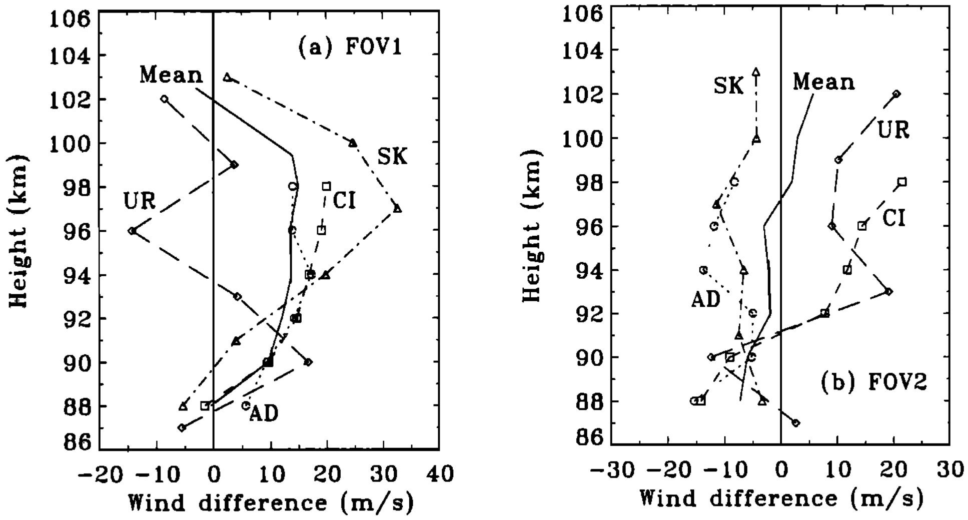

Figure 13. Average wind differences (WINDII – MF radar) for four ground stations, resolved in the directions of (a) FOV1 and (b) FOV2. The solid lines are the means of the four curves representing the individual stations, identified as follows: AD, Adelaide; CI, Christmas Island; SK, Saskatoon; UR, Urbana. The standard error is approximately ±5 m s^{-1} for Adelaide and ±10 m s^{-1} for the other stations.

Since WINDII has two fields of view with slightly different characteristics, it is essential to perform this comparison using line-of-sight winds. Therefore before zonally averaging the HRDI data, the meridional and zonal wind components are first projected onto WINDII's two line of sight directions. Figure 15 showsscatter plots of WINDII and HRDI line-of-sight winds for FOV1 and FOV2 at 100 km for three different days. The plotted points are for HRDI and WINDII "coincident" measurements along the same orbital track that are separated in space by no more than 300 km. In view of the fact that different emission lines each having different vertical distributions are being observed, that different techniques have been used in determining the inverted wind, and that the two instruments are not measuring exactly the same volume of atmosphere, it is not surprising that there is a certain degree of scatter in the figures. But the data points are scattered along the diagonals of unit slope and do not indicate an amplitude bias between WINDII and HRDI. Figure 16 shows scatterplots of the line-of-sight winds for the entire 2-year matching data set. The points are tightly packed along the diagonal and exhibit less scatter than the individual days.

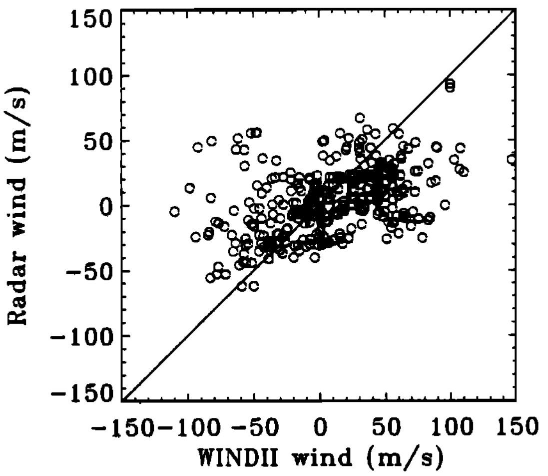

Figure 14. Scatter diagram for WINDII/MF radar comparisons for Adelaide for the 92-to-94-km altitude range. Data from the two fields of view are plotted together.

Systematic height-dependent differences between the wind measured by WINDII's two fields of view and by HRDI are obtained by averaging the multiday mean difference fields from 40°S to 40°N. The resulting curves (solid) are shown in Figure 17 for both the latitudinal mean differences and the standard deviations about the latitudinal means. Throughout the 95-to-110-km altitude range the differences between WINDII and HRDI are within 10 m s^{-1}. In addition, the two FOVs are seen to exhibit quite different height variations. The dashed curves in Figure 17 were obtained by shifting the HRDI data 1 km in the vertical with respect to WINDII. When HRDI is lowered 1 km, the agreement between the the two instruments is seen to improve significantly. This is particularly evident in Figures 17c and 17d where the deviations about the latitudinal means are much less. The oscillatory behavior in these two panels results from the presence of the meridional wind component of the diurnal tide which is antisymmetric about the equator. An altitude offset between two instruments viewing such a tidal wind field will result in a cell-like difference pattern which, upon latitudinal averaging, will produce the oscillations seen in Figures 17c and 17d. Thus in

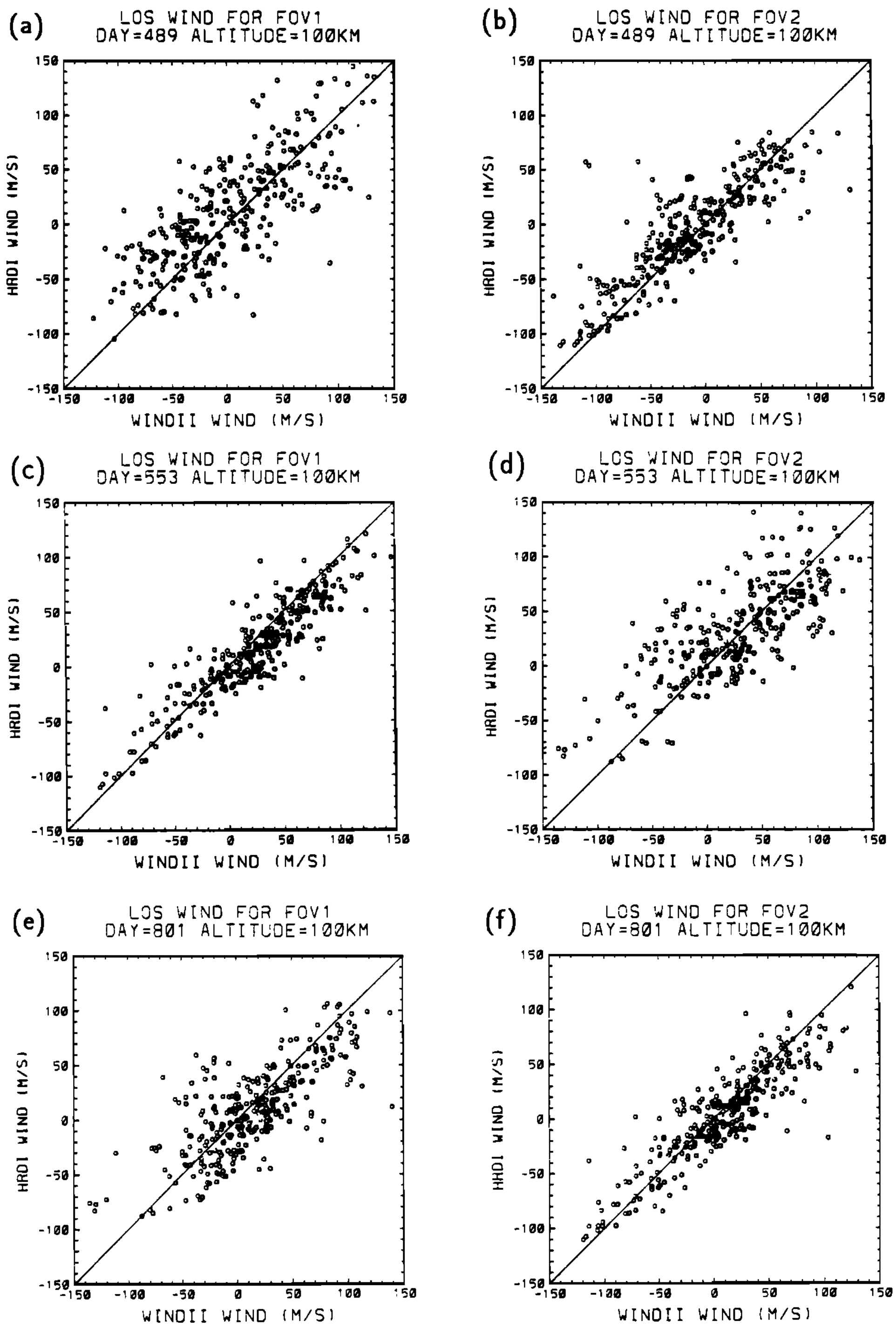

Figure 15. Scatterplots of the WINDII and high resolution Doppler imager (HRDI) line of sight winds at 100 km for (a) FOV1 and (b) FOV2 for January 12, 1993; (c) FOV1 and (d) FOV2 for March 17, 1993; and (e) FOV1 and (f) FOV2 for November 20, 1993. The diagonal solid line has unit slope.

addition to a small zero wind offset between WINDII and HRDI there is apparently a systematic 1-km altitude shift. We note from section 4.5 that the WINDII altitude determination is accurate to better than 1 km.

The final part of this section involves a comparison to HRDI's nighttime wind data which are provided at a single altitude that corresponds to the peak of emission layer which is generally about 94 km. Although HRDI's nighttime wind data are not inverted, it is still informative to compare them to WINDII's inverted winds. To do this, the individual HRDI 94-km nighttime measurements were projected onto WINDII's line-of-sight directions and then zonally averaged. Since the WINDII nighttime green line measurements occur half as fre-

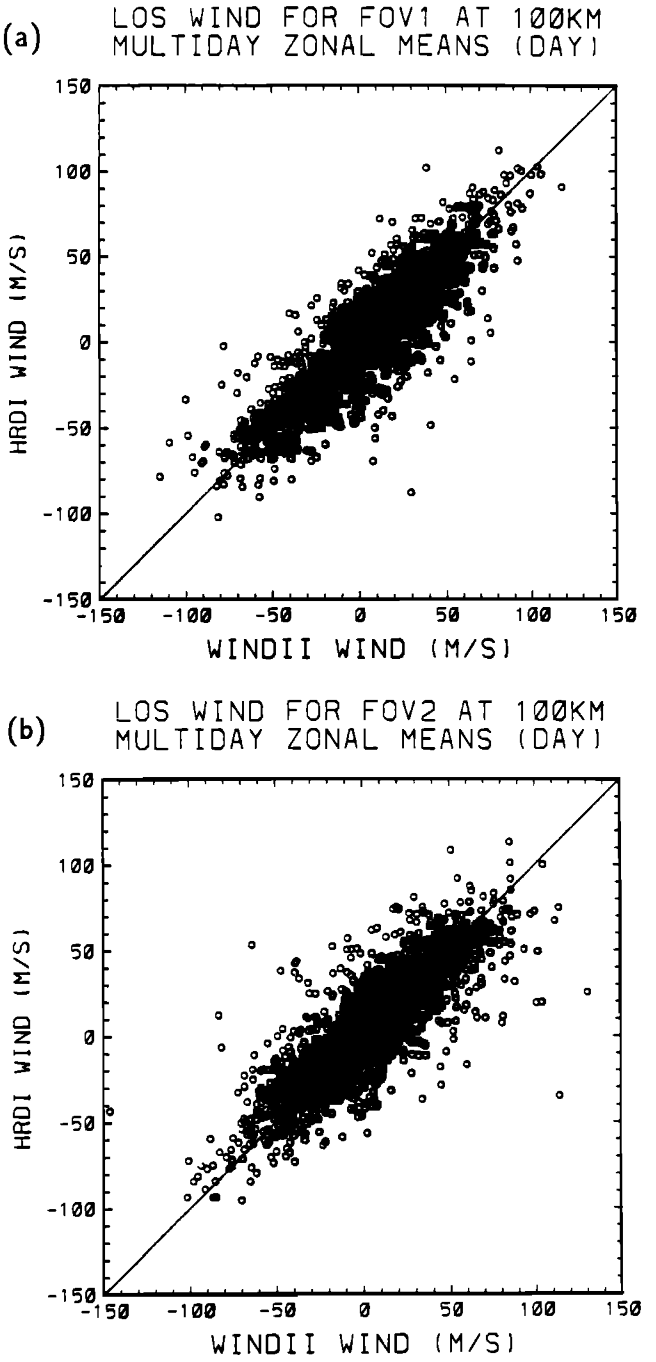

Figure 16. Scatterplots of the WINDII and HRDI zonal mean line of sight daytime winds at 100 km using the 2-year matching dataset for (a) FOV1 and (b) FOV2. Each circle denotes the zonal mean at a particular latitude for either the ascending or the descending orbits. The diagonal solid line has unit slope.

quently as the daytime, the number of comparable data points is less. The mean of the nighttime data are obtained in the same manner as for the daytime and the resulting scatterplots of the zonal means at 94 km are shown in Figure 18. As in the case of the daytime winds, the slope of the best fit curve through the data points (not drawn) appears to be very close to the line with unit slope, indicating no amplitude bias.

To determine a single value for the nighttime offsets, the mean differences over the 2-year period are averaged from 30°S to 30°N as in the daytime case. The resulting differences between WINDII and HRDI are 2.8 m s^{-1} and 3.2 m s^{-1} for FOV1 and FOV2, respectively.

7. Thermospheric O^1D and O^1S Winds

There was no laboratory source of O^1D emission available for prelaunch calibrations, so WINDII was launched without a zero phase reference for the ^1D channel. To provide a zero reference, several days were scheduled for interlacing $^1D/^1S$ measurements. If both emissions see the neutral wind, then the average of many alternating wind measurements should be the same for both and in that way the zero reference for ^1S can be extended to ^1D. Initially, data from two days were used and the CDB for ^1D was adjusted accordingly. The ^1D winds generated by version 4.23 of the software used this calibration. Subsequently, data were acquired from seven more days, and the averaged data from all nine days indicate that small corrections should be made to the zero reference for ^1D. Table 8 gives the average phase differences for the nine days. The ^1S phase has been scaled by the factor 0.882 to account for the different order of interference at the shorter wave-

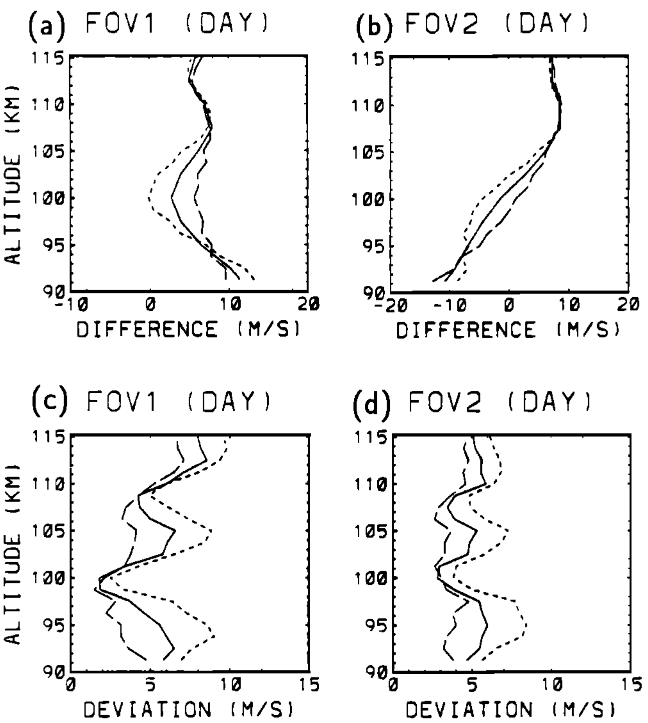

Figure 17. Latitudinal averages from 40°S to 40°N of the mean daytime line-of-sight wind differences for the 2-year matching dataset: WINDII - HRDI differences for (a) FOV1 and (b) FOV2; standard deviation of mean differences about the latitudinal mean for (c) FOV1 and (d) FOV2. The short-dashed curves are for HRDI raised by 1 km with respect to WINDII, the long-dashed curves are for HRDI lowered by 1 km, and the solid curves using the actual HRDI data.

Table 8. ^{1}S – ^{1}D Phase Differences for Interlaced Measurements

	Phase Difference $(0.882 \times \phi_{^1S} - \phi_{^1D})$	
	FOV1, deg	FOV2, deg
-1.5ex] Mean	1.03	0.64
s.d.	0.27	0.49
Range	0.5 to 1.4	0.1 to 1.9

length. The corresponding corrections which should be applied to the version 4.23 winds measured in the ^{1}D emission are +11.4 m s^{-1} for FOV1 and +7.3 m s^{-1} for FOV2. Subsequent production runs will include these corrections. The averaged profiles are shown in Figure 19, after the corrections were applied. The phase data are apparent quantities, prior to inversion, and the heights refer to the tangent point of the line of sight at the limb.

The height range used for matching the phases extends from 160 km, just below the peak of the ^{1}D emission, up to 230 km. In this range it is believed that the two emissions experience the same wind. The data are from daytime measurements between latitudes of 40° N and 40° S. At night the ^{1}S emission is generally very weak and its behavior not yet understood, so nighttime data were not used. The day/night phase differences are known from characterization measurements.

Section 2.3 describes how the zero phase reference determined near the bottom of the field of view was extended throughout the field by using a rubidium line close in wavelength to the ^{1}S emission. The same was done for the ^{1}D channel using a neon line, but this was a relative measurement because of the lack of a O^{1}D source. A residual horizontal variation of ±1° was revealed in both channels by averaging many measurements and it is reasonable to ask if a similar variation might exist in the vertical direction. This is not so easy to determine as for the horizontal case, because vertical wind structures could still be present after averaging.

The average phase plots in Figures 19a and 19b, however, show very similar behavior for the ^{1}D and ^{1}S emissions nearly to the top of the curves in FOV1 and up to 230 km in FOV2, where the agreement is within about 0.5°, or 5 m s^{-1}. This is evidence that any residual phase error in the vertical direction is within reasonable limits, as the two channels would not be expected to have the same errors. The other piece of evidence that supports the zero reference calibration in the thermosphere is the EISCAT comparison, which shows agreement within 3.5 m s^{-1} at 170 km for the meridional component measured in the ^{1}S emission.

In the top portion of the apparent phase measured in ^{1}S, the curve frequently bends over toward high negative values. This is seen in Figure 19b above 230 km. The effect can be present in both fields of view, in the averages of individual days and for all times of the year. Its cause is not yet understood. The effect takes place where the emission rate is low, so it does not have a great effect on the derived winds below this level. It is not likely due to a wind because it is always directed away from the spacecraft and it does not appear in the O^{1}D emission in the same region. If it were caused by

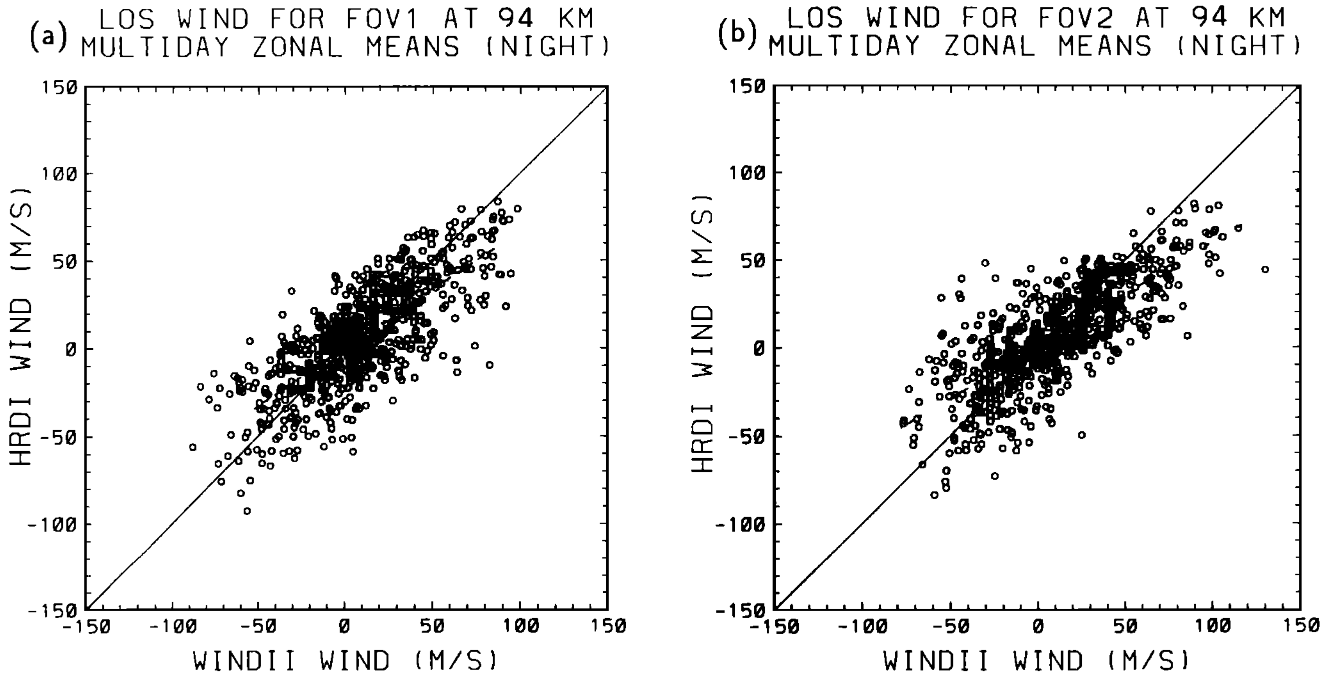

Figure 18. Scatterplots of the WINDII and HRDI zonal mean line-of-sight nighttime winds between 90 and 94 km using the 2-year matching data set for (a) FOV1 and (b) FOV2. The diagonal solid line has unit slope.

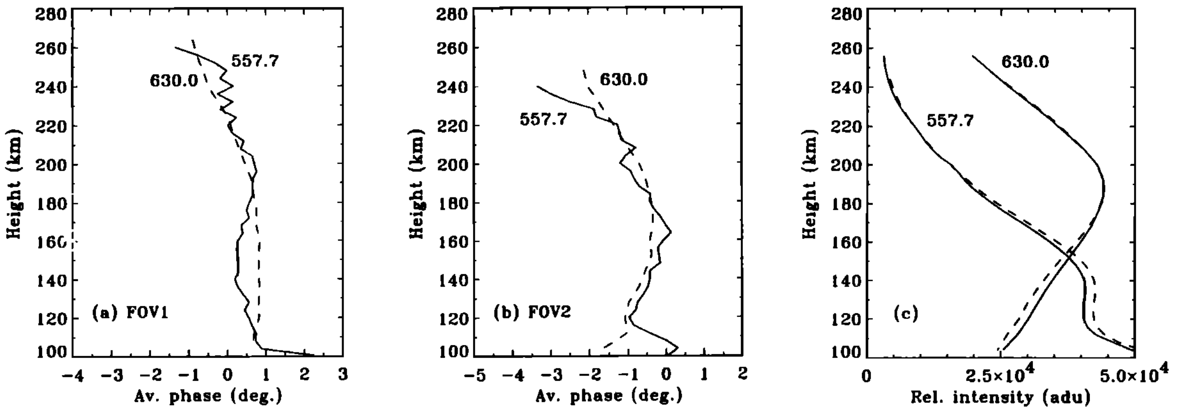

Figure 19. Averaged data for O^1S and O^1D for 9 days of interlaced measurements. (a and b) Apparent phase in FOV1 and FOV2, respectively, after the corrections from Table 8 have been applied to the ^1D phase. Solid lines are for O^1S, dashed lines for O^1D. The ^1S phase has been multiplied by 0.882 to allow for the different order of interference at the two wavelengths. (c) Averaged apparent intensities. Solid lines are for FOV1, dashed lines for FOV2.

an asymmetry in the shape of the emission line, the effect should, on average, be the same in both fields of view, but this is usually not so. Most likely it is an instrumental effect, and it does appear to be correlated with the amount of scattered light in the field of view, but it is not clear why the background level would affect the phase in this way.

8. Summary of Wind Comparisons

Sections 5 and 7 describe the validation efforts to date in comparing winds measured by WINDII in the O ^1S emission with those measured by ground-based optical interferometers, radars, and by HRDI. The results are summarized here in Table 9. In the table the error values given in columns 2 and 3 are the standard errors, i.e., $s/\sqrt{N}$, where s is the standard deviation and N is the number of comparisons. Column 4 gives the smallest difference which is statistically significant at the 90% confidence level (the probabilities of rejecting a true hypothesis and of accepting a false hypothesis are both 10%). The value given is the mean for the two fields of view. The MF radar results are means of data which come from four stations among which differences exist, so the statistical parameters are not listed. Approximate values for three of the individual stations are ±10 m s^{-1} for the standard error and 30 m s^{-1} for the confidence interval, with the fourth station (Adelaide) at about half these values. The WINDII-HRDI comparisons are latitudinal averages rather than one-to-one comparisons.

The original goal was to determine the zero wind ref-

Table 9. Summary of Wind Comparisons

Comparison	Wind Differences ± Standard Error FOV1, m s^{-1}	FOV2, m s^{-1}	90% Confidence Interval, m s^{-1}
WINDII-MICADO	9.2±4.1	8.9±3.6	±11.4
WINDII-Mount John FPI	8.1±4.9	-0.4±5.0	±14.7
WINDII-Peach Mountain FPI	4.0±5.1	-5.8±5.4	±15.4
WINDII-HRDI, night, 94 km	2.8	3.2	
WINDII-HRDI, day, 95 km	5.9	-7.4	
WINDII-MF radars, 95 km	13	1	
	Zonal Component	Meridional Component	
WINDII-EISCAT, 100 km	-9.0±11.7	4.7±7.7	±31.1
WINDII-EISCAT, 170 km		3.5±5.7	±18.5

erence to within ±10 m s^{-1}. None of the confidence intervals for the ground stations is as small as 10 m s^{-1}, though WINDII-MICADO is very close. This means that none of the comparison stations can, alone, be used to declare that the goal has been met at the 90% confidence level. It will be necessary to collect data from more passes in order to do that. However, the agreement among the data from the various ground stations and from HRDI is remarkably good, and taken in combination give a convincing demonstration that the zero reference for WINDII is known within 10 m s^{-1}.

The first four rows of Table 9 refer to data measured at night. For FOV1 the results are very consistent, suggesting that WINDII has a slight positive bias. The mean HRDI nighttime results in the table are for 94 km, just below the average peak of the ^{1}S emission. Adjusting the WINDII wind by -6 m s^{-1} brings agreement within ±3 m s^{-1}. For FOV2 the results are spread a little more and the values are both positive and negative. Adjusting WINDII by -1 m s^{-1} produces agreement within ±8 m s^{-1}. The FPI results suggest a difference between FOV1 and FOV2 of about 9 m s^{-1}, but MICADO and HRDI show little difference between FOV1 and FOV2.

Taking the three ground-based optical stations as a group, with equal weight given to each station, the mean differences are 7.1 and 0.9 m s^{-1} for FOV1 and FOV2, respectively. If equal weight is given to each individual measurement, the means are 7.1 and 1.9 m s^{-1}, and the 90% confidence interval is reduced to ±8.0 m s^{-1}. However, this procedure of mixing measurements from different stations might not be strictly valid, since differences in observing conditions and reduction methods might influence the result.

In the daytime, ground-based optical measurements are not available, leaving comparisons with radar and HRDI. The MF radar results are a mixture of day and night measurements but are heavily weighted to the daytime (section 5.4) and as yet have not been separated for comparison with WINDII. The overall mean in FOV1 is between 10 and 15 m s^{-1} from 90 to 100 km and in FOV2 it lies between 0 and 5 m s^{-1} from 92 to 100 km. This agrees well with the other results but is perhaps fortuitous in view of the large spread in the results from the MF radar stations. The WINDII-HRDI comparison at 95 km suggests a difference between the two fields of view of 13 m s^{-1}.

The meridional and zonal comparisons are shown for interest, though it is the components along the fields of view that are most important for validation purposes. The EISCAT measurements at 170 km are, however, our only comparisons in the upper ^{1}S emission region, and it is gratifying that the agreement is very good. As the satellite is near the northernmost point of its orbit during WINDII's EISCAT passes, the fields of view are oriented about 45° to the meridian, and FOV1 and FOV2 contribute approximately equally to the measurement of both zonal and meridional wind components. With this approximation, one can deduce average differences of 10 and -3 m s^{-1} for FOV1 and FOV2, respectively, based on the EISCAT data for 100 km, with a standard error of ±10 m s^{-1}. This is close to the other daytime differences, which are given for 95 km in Table 9.

In summary, all of the comparisons reported in Table 9 give an average difference in the wind zero reference of 10 m s^{-1} or less, except for the MF radars in FOV1. But these radars show a large spread in the results from individual stations, and it is felt that the relationship between the WINDII and the MF radar measurements is not yet understood. We believe that the data presented here show that WINDII's zero wind reference for the ^{1}S emission is correct within ±10 m s^{-1}, and no adjustment will be made at this time. This does not preclude small corrections being made at a later date, when more validation data have been analyzed.

Figure 17 indicates a possible difference of ~1 km between the WINDII and the HRDI altitude scales and a variation with altitude of the zero reference. These are not well understood at present, and studies are continuing. The possibility of an uncorrected time dependence of the zero reference is also being investigated. Future work will include validation of winds determined from the other emissions observed by WINDII. The validation will also be extended to include temperatures.

Acknowledgments. The WINDII project is sponsored by the Canadian Space Agency and the Centre National d'Etudes Spatiales; the authors are grateful for their continuing support. Additional assistance for validation and for scientific analysis of the data is provided by the Centre National de la Recherche Scientifique and the Natural Sciences and Engineering Research Council of Canada. The Institute for Space and Terrestrial Science, a designated Centre of Excellence supported by the Technology Fund of the Province of Ontario, also contributed to the activity described here. The investigations at Mount John Observatory are supported by National Science Foundation grant ATM-9300274. The observations at Peach Mountain Observatory are supported by National Science Foundation grant ATM-9301867 and NASA grant NAG1-1315. The EISCAT facility is supported by the research councils of Finland (SA), France (CNRS), the Federal Republic of Germany (MPG), Norway (NAVF), Sweden (NFR), and the United Kingdom (SERC). We are indebted to many other individuals who made major contributions to the WINDII validation but who are not named as coauthors. Among these are members of the WINDII Validation Committee, chaired by R.P. Lowe.

References

Bouchareine, P., and P. Connes, Interferometer with compensated field for Fourier transform spectroscopy, *J. Phys.*, *24*, 134-138, 1963.

Fauliot, V., G. Thuillier, and M. Hersé, Observations of the F-region horizontal and vertical winds in the auroral zone, *Ann. Geophys.*, *11*, 17-28, 1993.

Fauliot, V., G. Thuillier, and M. Hersé, Observations of the

E-region horizontal winds in the auroral zone and at mid-latitudes by ground-based interferometry, *Ann. Geophys.*, in press, 1994.

Forbes, J.M., and F. Vial, Monthly simulations of the solar semi-diurnal tide in the mesosphere and lower thermosphere, *J. Atmos. Terr. Phys.*, *51*, 649-662, 1989.

Forbes, J. M., R. G. Roble, and C. G. Fesen, Acceleration, heating, and compositional mixing of the thermosphere due to upward propagating tides, *J. Geophys. Res.*, *98*, 311-321, 1993.

Hays, P. B., V. J. Abreu, M. E. Dobbs, D. A. Gell, H. J. Grassl, and W. R. Skinner, The high resolution Doppler imager on the Upper Atmosphere Research Satellite, *J. Geophys. Res.*, *98*, 10,713-10,723, 1993.

Hersom, C., and G.G. Shepherd, Characterization of the Wind Imaging Interferometer, *Appl. Opt.*, *34*, 2871-2879, 1995.

Hilliard, R.L., and G.G. Shepherd, Wide-angle Michelson interferometer for measuring Doppler line widths, *J. Opt. Soc. Am.*, *56*, 362, 1966.

Lilensten, J., G. Thuillier, C. Lathuillere, W. Kofman, V. Fauliot, and M. Hersé, EISCAT-MICADO coordinated measurements of meridional wind, *Ann. Géophys.*, *10*, 603-618, 1992.

Manson, A. H., C. E. Meek, H. Teitelbaum, F. Vial, R. Schminder, D. Kurschner, M. J. Smith, G. J. Fraser, and R. R. Clark, Climatologies of semi-diurnal and diurnal tides in the middle atmosphere (70-110 km) at middle latitudes (40-55°), *J. Atmos. Terr. Phys.*, *51*, 579-593, 1989.

Massebeuf M., R. Bernard, J.L. Fellous, and M. Glass, Simultaneous meteor radar observation at Monpazier (440 N) and Punta Boriquen (180 N), II, Mean zonal wind and long period waves, *J. Atmos. Terr. Phys.*, *43*, 535-542, 1981.

McLandress, C., Y. Rochon, G. G. Shepherd, B. H. Solheim, G. Thuillier, and F. Vial, The meridional wind component of the thermospheric tide observed by WINDII on UARS, *Geophys. Res. Lett.*, *21*, 2417-2420, 1994.

Menke, W., *Geophysical Data Analysis: Discrete Inverse Theory*, Academic, San Diego, Calif., 1984.

Rodgers, C.D., Retrieval of atmospheric temperature and composition from remote measurements of thermal radiation, *Rev. Geophys.*, *14*, 609-624, 1976.

Rodgers, C. D., Characterization and Error Analysis of Profiles Retrieved From Remote Sounding Measurements, *J. Geophys. Res.*, *95*, 5587-5595, 1990.

Shepherd, G.G., et al., Longitudinal structure in atomic oxygen concentrations observed with WINDII on UARS, *Geophys. Res. Lett.*, *20*, 1303-1306, 1993a.

Shepherd, G.G., et al., WINDII the Wind Imaging Interferometer on the Upper Atmosphere Research Satellite, *J. Geophys. Res.*, *98*, 10,725-10,750, 1993b.

Shepherd, G.G.,C. McLandress, and B.H. Solheim, Tidal influence on O(^{1}S) airglow emission rate distributions at the geographic equator as observed by WINDII, *Geophys. Res. Lett.*, *22*, 275-278, 1995.

Taylor, M.J., M.A. Hapgood, and P. Rothwell, Observations of gravity wave propagation in the OI (557.7 nm), Na (589.2 nm), and the near infrared OH nightglow emissions, *Planet. Space Sci.*, *35*, 413-427, 1987.

Thuillier, G., and M. Hersé, Thermally stable field compensated Michelson interferometer for measurement of temperature and wind of the planetary atmospheres, *Appl. Opt.*, *30*, 1210-1220, 1991.

Thuillier, G., and G.G. Shepherd, A fully compensated Michelson interferometer of fixed path difference, *Appl. Opt.*, *24*, 1599-1603, 1985.

Thuillier, G., C. Lathuillere, M. Hersé, C. Senior, W. Kofman, M.-L. Duboin, D. Alcayde, F. Barlier, and J. Fontanari, Co-ordinated EISCAT-MICADO interferometer measurements of neutral winds and temperatures in E-and F-regions, *J. Atmos. Terr. Phys.*, *52*, 625-636, 1990.

Thuillier G., V. Fauliot, M. Hersé, L. Bourg, and G.G. Shepherd, The MICADO wind measurements from Observatoire de Haute-Provence for the validation of the WINDII green line data, *J. Geophys. Res.*, this issue.

Twomey, S., *Introduction to the Mathematics of Inversion in Remote Sensing and Indirect Measurements*, *Dev. Geomath. Ser.* Elsevier, New York, 1977.

Ward, W. E., The design and implementation of a wide-angle Michelson interferometer to observe thermospheric winds, Ph.D. thesis, 373 pp., York University, Toronto, Ontario, Canada, 1988.

Wiener, N., Generalized harmonic analysis, *Acta Math.*, *55*, 117-258, 1930.

L. Bourg, V. Fauliot, M. Hersé, and G. Thuillier, Service d'Aéronomie, B.P. No. 3, 91371 Verrières-le-Buisson Cedex, France

M.D. Burrage and R. Niciejewski, Space Physics Research Laboratory, University of Michigan, Ann Arbor, MI 48109

S.J. Franke, University of Illinois, Urbana, IL 61801

R.L. Gattinger, Herzberg Institute of Astrophysics, National Research Council of Canada, Ottawa, Ontario, Canada K1A 0R6.

W.A. Gault (corresponding author), Y.J. Rochon, G. G. Shepherd, B.H. Solheim, R.H. Wiens and Z.P. Zhang, York University, 4700 Keele Street, North York, Ontario, Canada M3J 1P3.

G. Hernandez, University of Washington, Seattle, WA 98011

C. Hersom, C. McLandress, C. Tai, W.E. Ward, Institute for Space and Terrestrial Science, 4850 Keele Street, North York, Ontario, Canada M3J 3K1

C. Lathuillere, Centre d'Etude des Phénomènes Aléatoires et Géophysiques, ENSIEG, B.P. No. 46, 38402 Saint-Martin-d'Hères Cedex, France

A. Manson, University of Saskatchewan, Saskatoon, Saskatchewan, Canada, S7N 0W0

R. Vincent, University of Adelaide, Adelaide 5001, Australia

(Received November 17, 1994; revised September 30, 1995; accepted September 30, 1995.)